

NASA CR - 135116



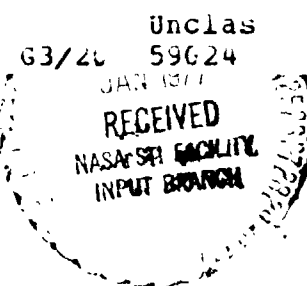
15 CM MERCURY ION THRUSTER  
RESEARCH - 1976

PREPARED FOR  
LEWIS RESEARCH CENTER  
NATIONAL AERONAUTICS AND SPACE ADMINISTRATION

GRANT NGR-06-002-112

(NASA-CR-135116) FIFTEEN CM MERCURY ION  
THRUSTER RESEARCH, 1976 ANNUAL REPORT, 1  
Dec. 1975 - 1 Dec. 1976 (Colorado State  
Univ.) 81 p HC A.5/ME A.1 CSCI 210

N77-17147



Annual Report  
December 1976  
Paul J. Wilbur  
Department of Mechanical Engineering  
Colorado State University  
Fort Collins, Colorado

ORIGINAL PAGE IS  
OF POOR QUALITY

1 Report No NASA CR-135116	2 Government Accession No.	3. Recipient's Catalog No	
4. Title and Subtitle 15 CM MERCURY ION THRUSTER RESEARCH - 1976		5. Report Date December 1976	6. Performing Organization Code
		8. Performing Organization Report No	
7. Author(s) Paul J. Wilbur		10. Work Unit No	
9 Performing Organization Name and Address Department of Mechanical Engineering Colorado State University Fort Collins, Colorado 80523		11. Contract or Grant No. NGR-06-002-112	
		13. Type of Report and Period Covered Dec. 1, 1975 - Dec. 1, 1976	
12. Sponsoring Agency Name and Address National Aeronautics and Space Administration Washington, D. C. 20546		14. Sponsoring Agency Code	
		15 Supplementary Notes Grant Monitor, William Kerslake Spacecraft Technology Div. NASA Lewis Research Center Cleveland, Ohio 44135	
16 Abstract Improvements in 15 cm diameter, SERT II, mercury ion thruster performance effected by the use of SHAG optics at 33 V discharge voltage are discussed. At a 200 eV/ion discharge power, 90% propellant utilization and 660 mA beam current operating condition a doubly-to-singly charged ion current ratio of about 4% is measured. Performance of the 15 cm multipole mercury thruster (optimized for length and the point of electron injection) is compared to that of divergent (SERT II) and cusped field designs and found to be comparable. The need for a magnetic baffle in the multipole thruster is identified and the preferred point of electron injection is shown to be at the upstream end of the discharge chamber. Results of preliminary tests on the effects of discharge voltage and total accelerating voltage on perveance and beam divergence characteristics of two grid ion optics are examined. Experimental data showing the effect of target temperature on sputtering rates in a mercury discharge environment are presented and a deficiency in the test procedure is identified. Errors in erosion rate measurements are related to the formation of protective cones on the multilayer erosion detectors employed for the test. Hollow cathode startup using radio frequency power is demonstrated. Temperatures within an operating hollow cathode are examined as a function of cathode orifice diameter, insert type, and insert location over a range of emission currents and cathode heater powers. It is observed that temperatures can be correlated with total power to the cathode and that insert and orifice plate temperature reductions of order 100°C can be effected through changes in insert type and location.			
17 Key Words (Suggested by Author(s)) Electrostatic Thruster Hollow Cathode		18 Distribution Statement Unclassified - Unlimited	
19 Security Classif (of this report) Unclassified	20 Security Classif (of this page) Unclassified	21. No of Pages 82	22 Price*

\* For sale by the National Technical Information Service Springfield Virginia 22161

## TABLE OF CONTENTS

	Page
Abstract . . . . .	i
Introduction . . . . .	1
Cusped Magnetic Field Thruster . . . . .	2
Model for Doubly Charged Ion Production in Mercury Ion Thrusters . .	2
Effects of Small Hole Accelerator Grid on SERT II Thruster Performance . . . . .	2
Apparatus . . . . .	3
Results . . . . .	4
Conclusions . . . . .	12
15 cm Multipole Mercury Thruster . . . . .	14
Apparatus and Procedure . . . . .	14
Results . . . . .	18
Thruster Length. . . . .	18
Cathode Location . . . . .	20
Discharge Current Distribution . . . . .	25
Discharge Stability . . . . .	30
Plasma Properties. . . . .	30
Doubly Charged Ions. . . . .	32
Conclusions . . . . .	34
Ion Optics Study . . . . .	35
Parameter Definitions . . . . .	35
Apparatus and Procedure . . . . .	35
Results and Discussion. . . . .	36
Conclusion. . . . .	41

<b>Effect of Target Temperature on Sputtering Rate. . . . .</b>	<b>42</b>
<b>Apparatus and Procedure . . . . .</b>	<b>42</b>
<b>Results . . . . .</b>	<b>45</b>
<b>Discussion and Conclusions . . . . .</b>	<b>48</b>
<b>Cathode Ignition Using Radio-Frequency Power . . . . .</b>	<b>51</b>
<b>Apparatus and Procedure . . . . .</b>	<b>51</b>
<b>Results . . . . .</b>	<b>54</b>
<b>Conclusion . . . . .</b>	<b>56</b>
<b>The Effect of the Insert on Hollow Cathode Temperatures. . . . .</b>	<b>57</b>
<b>Apparatus and Procedure . . . . .</b>	<b>57</b>
<b>Results . . . . .</b>	<b>61</b>
<b>Conclusions . . . . .</b>	<b>69</b>
<b>Appendix A - Magnetic Baffle for 15 cm Multipole Mercury Thruster. .</b>	<b>70</b>
<b>Baffle Design . . . . .</b>	<b>71</b>
<b>Testing . . . . .</b>	<b>71</b>
<b>Results . . . . .</b>	<b>73</b>
<b>References . . . . .</b>	<b>76</b>

## INTRODUCTION

The discharge chamber work carried out during this report period has led to some understanding of the functions served by magnetic fields which lends itself to the following generalization. The magnetic field shape and its proximity to anode and screen grid surfaces serves the three separable functions of 1) defining the region in which the bulk of the ionizations occur (primary electron region) and the shape of the ion beam profile, 2) determining the plasma properties in this region and 3) determining the impedance in the baffle aperture region. A possible fourth function associated with discharge oscillations has not studied so it will not be commented upon.

The concept of a critical magnetic field line passing from the downstream end of the cathode pole piece to the anode pole piece, as suggested by King, et al.,<sup>[1]</sup> has been substantiated by Beattie<sup>[2]</sup> in a number of experiments. This work has shown that the bulk of the ionizing reactions occur between the surface of revolution of the critical field line and the screen grid and that the distance between this surface of revolution and the screen grid at a given radius determines the relative ionization probability at that radius. The uniformity of the critical field line - screen grid separation distance as a function of radius thereby determines the flatness of the ion beam profile.

The plasma properties within the primary electron region are determined by the proximity of the critical field line and the anode at their closest separation distance. This interrelationship was demonstrated by Beattie<sup>[2]</sup> through the use of an anode which could be moved closer to or further away from the critical field line during thruster operation to produce corresponding decreases or increases in Maxwellian electron temperature and primary electron energy.

Studies, reported herein by Longhurst, have confirmed earlier work by Well's [3] which showed that the magnetic field within the cathode pole piece in the vicinity of the baffle aperture impedes electron flow from the cathode discharge to the main discharge regions of the thruster. In the multipole thruster, where the baffle aperture could be moved into regions of the discharge chamber having low magnetic field intensities in the direction across the aperture, it was observed that voltage differences could not be sustained across the aperture by a simple geometrical means. A magnetic field across the aperture was essential to proper discharge chamber operation.

#### CUSPED MAGNETIC FIELD THRUSTER

The work accomplished on this device during the grant period is described in detail in Reference [2] and it will not be reproduced here.

#### MODEL FOR DOUBLY CHARGED ION PRODUCTION IN MERCURY ION THRUSTERS

The development and experimental verification of this model is described in detail in Reference [4] and it will not be reproduced here.

#### EFFECTS OF A SMALL HOLE ACCELERATOR GRID ON SERT II THRUSTER PERFORMANCE

Small Hole Accelerator Grid (SHAG) optics have been shown to be effective in increasing the propellant utilization efficiency of ion thrusters [5]. This occurs because the accelerator grid open area is reduced with the hole diameter, thereby reducing the effective area for the

loss of neutral propellant atoms while leaving the effective open area for the loss of ions (the screen grid open area) unaltered. It is also possible to reduce the discharge voltage in a thruster which employs SHAG optics to reduce the doubly charged ion density in the discharge chamber, and while this results in a performance degradation, performance with SHAG optics, at the lower discharge voltage, is generally better than that observed with the larger hole accelerator grid system operating at the higher discharge voltage, where doubly charged ion densities are excessive. The extent to which thruster performance can be improved and doubly charged ion densities can be reduced in a 15 cm diameter mercury thruster through the application of SHAG optics had not been investigated. The present study was therefore initiated to determine the extent of these effects.

#### Apparatus

A SERT II thruster<sup>[6]</sup> was modified to include independent main and hollow cathode flow control and measurement systems, electromagnets, a solid disc baffle, and a 0.5 mm dia. orifice hollow cathode for the tests described herein. All grid sets used in this comparative study were dished downstream and all employed the same screen grid but the aperture diameter and thickness of the accelerator grid were varied. Tests were run at an accel grid potential of -0.5 kV and screen grid potentials of both +1 kV and +1.5 kV. The dimensions of the grids used in the study are given in Table I.

Faraday and E x B momentum analyzer probes used to measure ion beam current density profiles and doubly-to-singly charged ion current density profiles in this study are described in References [7] and [8] respectively.

Table I. Grid Dimensions

	Open Area Fraction	Aperture Diameter	Center-to-Center hole Spacing	Thickness	Cold Separation Distance
Screen	67%	1.91 mm	2.21 mm	0.38 mm	0.79 mm
Accel	67%	1.91 mm	2.21 mm	0.38 mm	
Screen	67%	1.91 mm	2.21 mm	0.38 mm	0.79 mm
Accel	54%	1.70 mm	2.21 mm	0.51 mm	
Screen	67%	1.91 mm	2.21 mm	0.38 mm	0.61 mm
Accel	24%	1.14 mm	2.21 mm	0.51 mm	

### Results

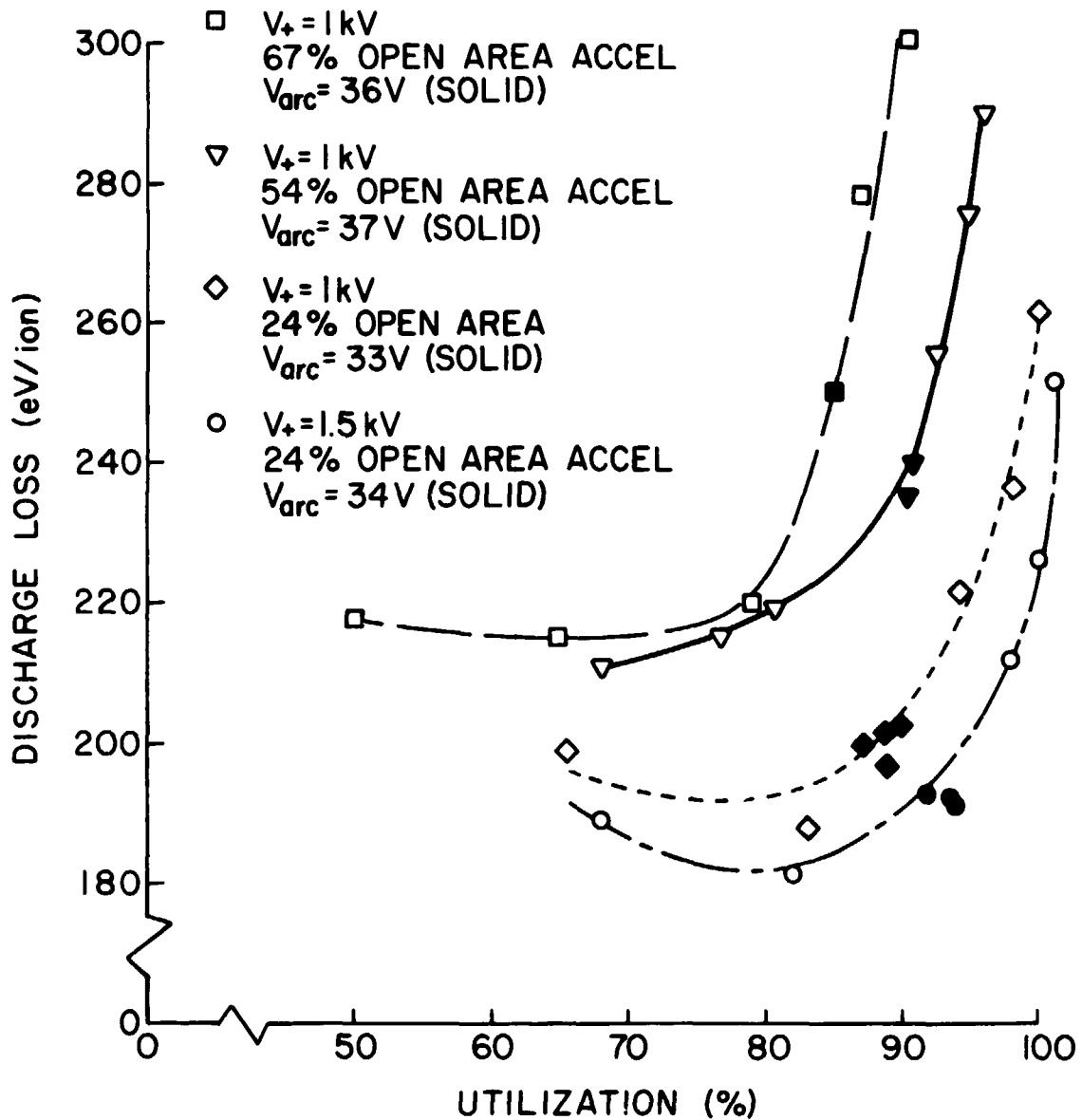
The effects of variations in the accelerator grid open area, discharge voltage level, and screen grid potential on beam ion production costs and propellant utilization efficiency are presented in Figure 1 for the SERT II discharge chamber operating at a nominal mercury flow rate of 740 mA. At the data points represented by the solid symbols, the discharge voltage ( $V_{arc}$ ) is equal to the value indicated in the legend for each curve. Data presented in these curves have not been corrected for the presence of doubly charged ions in the beam because doubly charged ion current measurements were made only at the operating conditions defined by the solid symbols.

Figure 1 shows the general tendency for improved performance of the thruster as accelerator grid open area fraction is reduced from 67% to 24%. The performance with 24% open area accel grid is seen to be significantly better than that obtained with the 54% open area grids even though

## SERT II THRUSTER

 $\dot{m} = 740 \text{ mA}$  $V_- = -0.5 \text{ kV}$ 

67% OPEN AREA SCREEN



SERT II THRUSTER PERFORMANCE COMPARISONS

FIGURE 1

the discharge voltage had been reduced from 37 V to 33 V for the 24% open area test. An increase in the screen grid potential accompanied by a small increase in discharge voltage was seen to effect a further improvement in performance with the 24% open area grids. The reduction in accelerator grid open area fraction from 67% to 24% accompanied by a discharge voltage reduction from 36 V to 33 V is observed to result in a 10% reduction in discharge losses and a 10% increase in propellant utilization at the knees of the performance curves.

Figure 2 presents data obtained with the SERT II thruster operated at a throttled flow condition (440 mA) with two different grid sets, two discharge voltages, and two different screen grid potentials. These results agree qualitatively with those observed at the higher flow rate condition of Figure 1. Reductions in accelerator grid open area, increases in discharge voltage and/or increases in screen grid potential all tend to improve performance. The substitution of 24% open area accel grid set for the 67% set is observed to effect an 8% increase in propellant utilization and a 25% reduction in discharge loss.

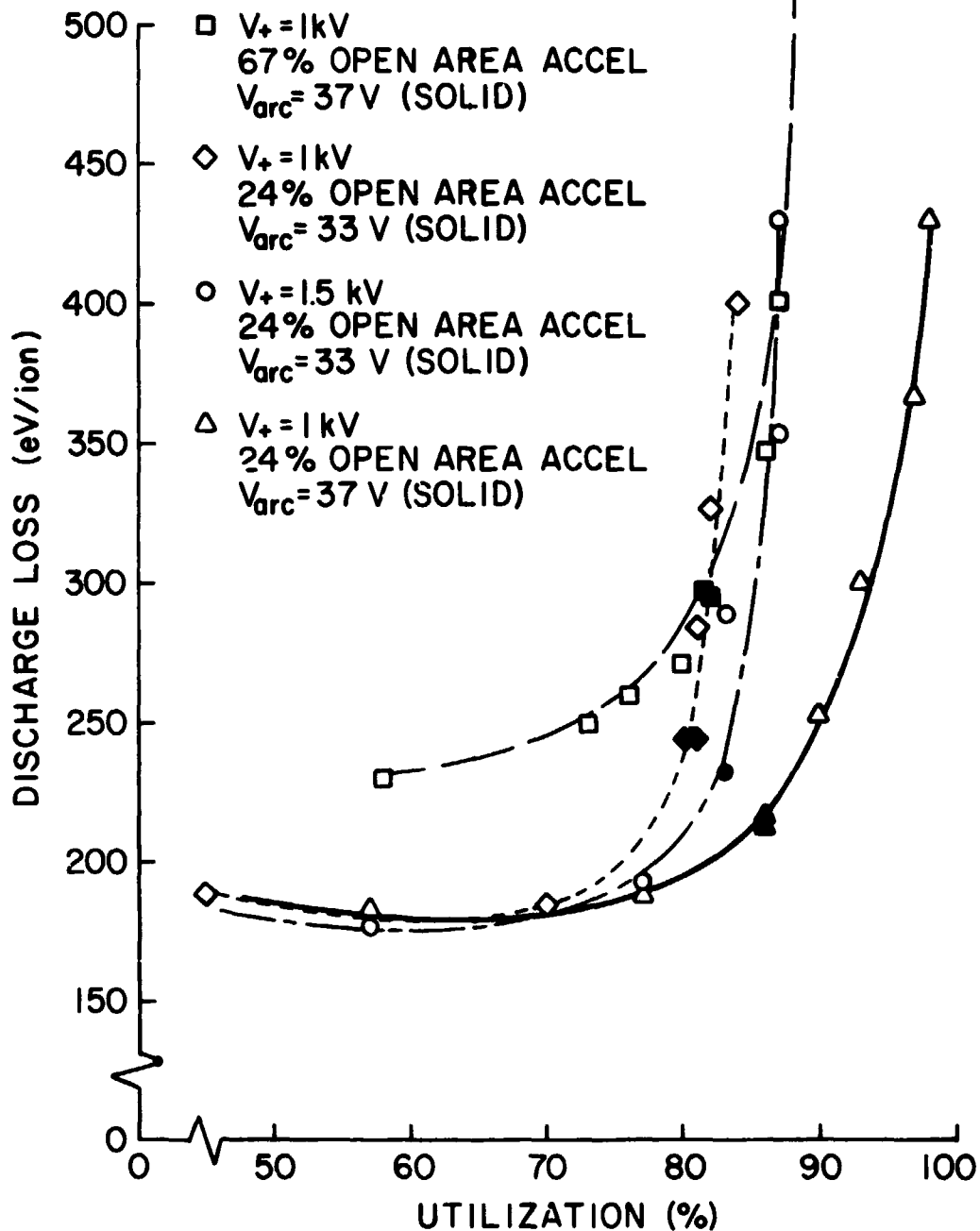
The effects of discharge voltage, accelerator grid open area, and screen grid potential on double-to-single ion current ratio and ion beam flatness, measured 6 mm downstream of the grids, are illustrated by the data of Table II. All of the data presented in this table correspond to the solid data points which are located near the knees of the curves of Figures 1 and 2 except for the data of Test No. 3. These test data were not plotted, even though they do fit as one would expect with the other data of Figure 1, because the mass flow rate was significantly less than the nominal 740 mA value of Figure 1. The doubly-to-singly charged beam

SERT II THRUSTER

$\dot{m} = 440 \text{ mA}$

$V_- = -0.5 \text{ kV}$

67% OPEN AREA SCREEN



SERT II THRUSTER PERFORMANCE COMPARISONS

(THROTTLED FLOW)

FIGURE 2

Table II

SERT II Thruster Performance Comparison

Test No.	Accel Grid Open Area	Screen Grid Potential	Mass Flow Rate	Discharge Current	Discharge Voltage	Beam Current	Discharge Loss	Utilization	I <sup>++</sup> /I <sup>+</sup>	F
1	67%	1 kV	734 mA	4.32 A	36.0 V	623 mA	250 eV/ion	85%	--	0.45
2	54%	1 kV	733 mA	4.06 A	37.5 V	654 mA	235 eV/ion	90%	8.1%	--
3	24%	1 kV	685 mA	4.0 A	36.2 V	650 mA	224 eV/ion	95%	8.2%	0.44
4	24%	1 kV	735 mA	4.0 A	33.3 V	660 mA	202 eV/ion	90%	3.8%	0.45
5	24%	1.5 kV	748 mA	4.0 A	33.5 V	691 mA	194 eV/ion	92%	4.5%	0.42
6	67%	1 kV	440 mA	2.7 A	37.0 V	354 mA	280 eV/ion	80%	--	0.46
7	24%	1 kV	439 mA	2.55 A	33.3 V	358 mA	238 eV/ion	82%	4.2%	0.46
8	24%	1.5 kV	437 mA	2.56 A	33.1 V	364 mA	233 eV/ion	83%	5.1%	0.46
9	24%	1 kV	438 mA	2.17 A	36.9 V	375 mA	214 eV/ion	86%	8.1%	0.45

ion current ratios given in column ten of Table II are seen to be significantly higher at the higher discharge voltage levels (Tests 2, 3 and 9). This observation agrees with Peters' theoretical study [4] which relates primary electron energy and electron temperature to discharge voltage and shows that increases in these two plasma properties result in increased production of doubly charged ions. A less pronounced effect is the increase in double-to-single ion current ratio which seems to accompany increases in screen grid potential. This effect appears to be related to increases in primary electron energy and Maxwellian electron temperature which accompany the slight increase in propellant utilization effected by the increase in screen grid potential. The nominal 4% double-to-single ion current ratio which occurs at a 33 V discharge condition with 24% open area accelerator grids corresponds to an average double-to-single ion density ratio in the discharge chamber of about 1.4%. If one assumes the screen grid erosion rate is directly proportional to the double ion density then the 280 Å/hr maximum erosion rate observed on the 30 cm thruster [9] at a measured double-to-single ion density ratio of approximately 6% [4] can be used to estimate a erosion rate that should be significantly less than 60 Å/hr on the SERT II screen grid. This value is sufficiently low to assure the screen grid will not erode to half of its original thickness in less than 30,000 hours.

Column eleven of Table II contains the flatness parameter associated with the ion beam current density profile measured 6 mm downstream of the center of the accelerator grid at the operating conditions defined by the solid symbols on Figures 1 and 2. The flatness parameter, which represents the ratio of average-to-peak current density in the ion beam, is seen to be only slightly higher at the lower flow rate condition. The data suggest

changes in discharge voltage, accelerator grid open area and screen grid potential do not affect the ion beam flatness significantly.

In an additional test the total flow rate to the 15 cm SERT II thruster employing the 24% open area accelerator grid was increased above the 740 mA flow rate which had given near optimum performance with the 67% open area accelerator grid. It was hoped that beam current density limitations imposed by the SHAG optics could be determined by doing this. During the test, discharge voltage was held near 33 V, by reducing the hollow cathode flow rate as the main flow rate was increased, discharge current was increased in proportion to beam current to maintain a constant discharge loss (eV/ion) and other voltages and currents such as the screen and accelerator voltages and the keeper current were held constant. Following this procedure at a screen voltage of 1.5 kV, a total flow rate of 880 mA and a corresponding beam current of 780 mA were achieved before the propellant utilization began to drop off significantly. Thruster performance observed at this flow condition is illustrated by the data of Figure 3 along with data obtained at a 1 kV screen grid potential at the same flow rate. The good performance observed at the nominal operating condition defined by the solid symbols on Figure 3 coupled with a measured double-to-single ion current density ratio near 5% suggest that the SERT II thruster should operate satisfactorily at a beam current of 780 mA with SHAG optics at screen and accel grid potentials of 1.5 kV and -0.5 kV respectively. The measured ion beam flatness parameter was degraded from a value near 0.45 at a 740 mA flow rate condition to about 0.43 at this higher flow rate.

Table III shows the average beam current density conditions corresponding to the nominal (solid) and maximum utilization operating points of Figure 3. These data suggest that average beam current densities approaching 5 mA/cm<sup>2</sup>

SERT II THRUSTER

$\dot{m} = 880 \text{ mA}$

$V_- = -0.5 \text{ kV}$

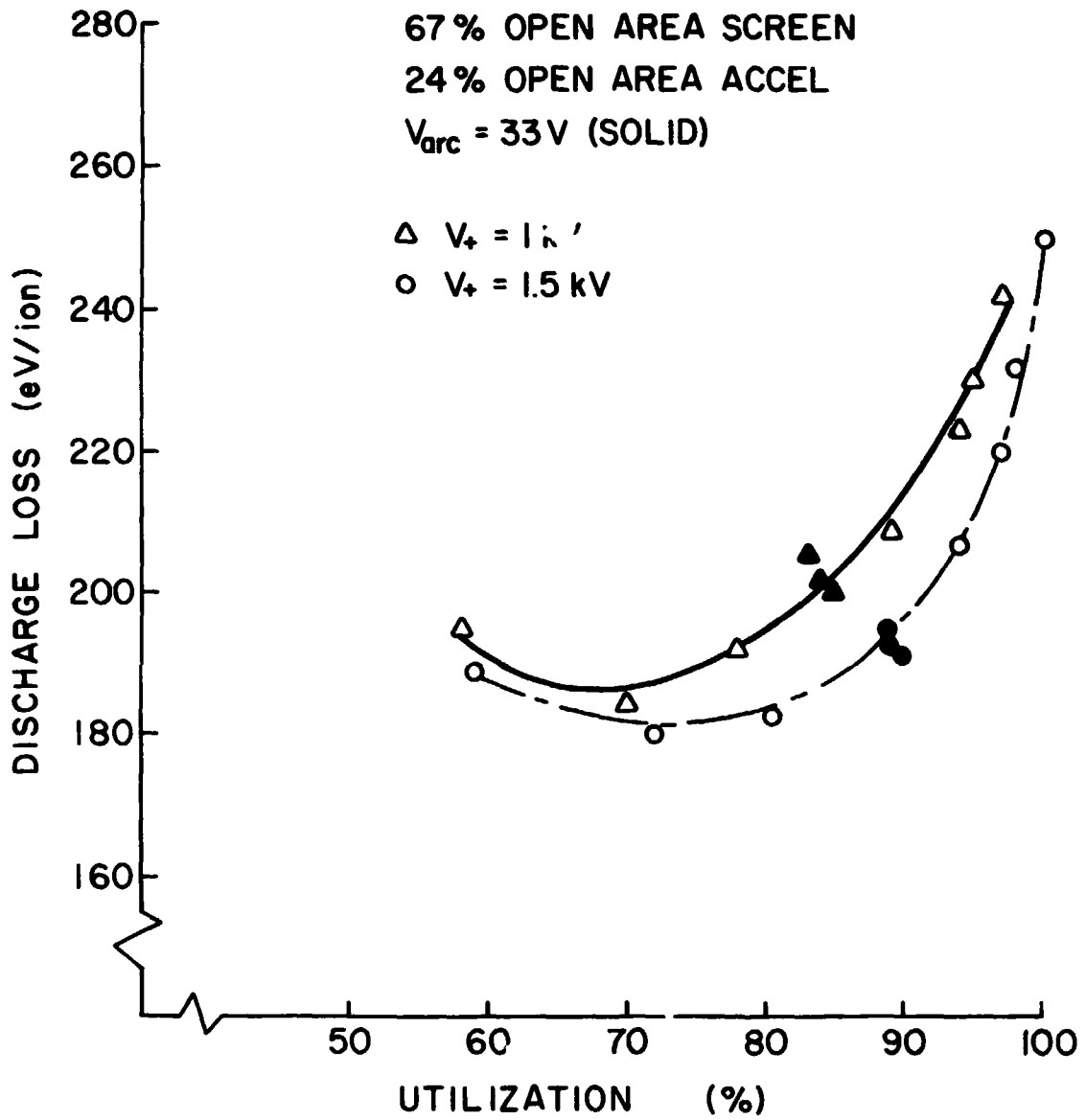
67% OPEN AREA SCREEN

24% OPEN AREA ACCEL

$V_{\text{arc}} = 33 \text{ V (SOLID)}$

$\Delta V_+ = 1 \text{ kV}$

$\circ V_+ = 1.5 \text{ kV}$



SERT II THRUSTER PERFORMANCE AT PEAK FLOW

FIGURE 3

represent a limit, beyond which a 15 cm thruster operating the 24% open area accelerator grid optics of Table I, begin to show a performance degradation. The average normalized perveance per hole corresponding to the data of Table III are about 0.9 nanopervs/hole at 1.5 kV screen potential and 0.6 nanopervs/hole at 1.0 kV. Peak perveance values which would occur at the center of the grids are estimated on the basis of the flatness parameters to be nearly twice as great.

Table III

15 cm Thruster Performance with SHAG Optics

at High (880 mA) Total Flow Rate

Screen Grid Potential	Discharge Voltage	Discharge Loss	Utilization	Beam Current	Average Beam Current Density
* 1 kV	33 V	202 eV/ion	84%	740 mA	4.2 mA/cm <sup>2</sup>
1 kV	33 V	242 eV/ion	97%	860 mA	4.8 mA/cm <sup>2</sup>
* 1.5 kV	33 V	193 eV/ion	89%	780 mA	4.4 mA/cm <sup>2</sup>
1.5 kV	34 V	250 eV/ion	99%	870 mA	4.9 mA/cm <sup>2</sup>

\* Nominal Steady State Operating Condition

### Conclusions

In the 15 cm diameter SERT II mercury ion thruster, substitution of a 24% open area accelerator grid for a 67% open area one accompanied by operation at 33 V rather than 36 V discharge voltage, results in about a 10% reduction in discharge losses and a 10% increase in propellant utilization at a propellant flow rate of 740 mA. The corresponding doubly-to-singly charged ion density ratio within the discharge chamber of the SHAG

optics thruster operating at this condition is about 1.4% and this should be sufficiently low to assure a screen grid lifetime of more than 30,000 hours.

The propellant flow rate into the SHAG optics thruster can be increased to about 880 mA at a beam current of about 750 mA before the thruster performance will begin to degrade with the 24% open area accelerator grid. Doubly charged ion density increases to about 1.8% and ion beam flatness decreases slightly as a result of this flow rate increase.

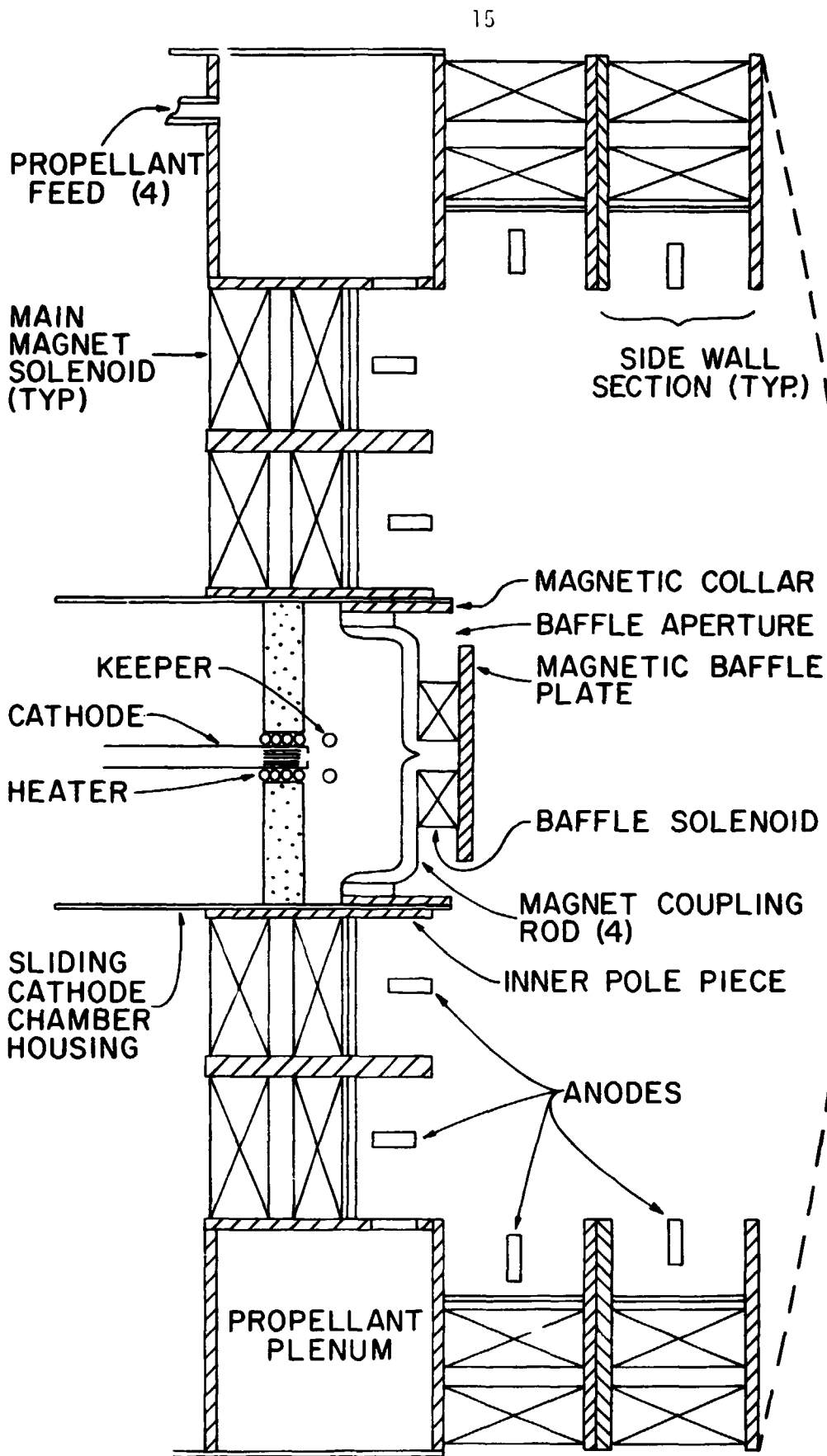
## 15 cm MULTIPOLE MERCURY THRUSTER

G. Reed Longhurst

The 15 cm diameter multipole thruster design has been reported by Isaacson and Kaufman<sup>[10]</sup> to operate efficiently using argon and xenon as propellants. Because this design shows considerable promise as a means of achieving efficient operation and flat ion beam profiles and because it can be scaled easily to various sizes, the present investigation of its performance using mercury as the propellant was undertaken. Data obtained in the study was to be compared with that obtained from other mercury thruster designs, particularly the divergent field thruster (SERT II) and the Cusped Magnetic Field (CMF) thruster investigated by Beattie.<sup>[2]</sup> Because the multipole design had not been operated on mercury and had not been operated using a hollow cathode electron source, some optimization of the chamber was required before meaningful comparisons could be made against other thruster designs. Design parameters which were varied during this optimization included the discharge chamber length, the magnetic field strength and the point of electron injection into the main discharge chamber from the cathode discharge chamber.

### Apparatus and Procedure

Figure 4 is a schematic drawing of the axisymmetric multipole thruster configuration used in this study. Proper operation of the device depends on the establishment of magnetic fields between pole piece pairs straddling each of the anodes shown in Figure 4. These anodes serve to remove low energy electrons from the discharge chamber as high energy (primary) electrons are resupplied from the cathode. The construction details of the side wall and upstream sections as well as the magnetic field intensities



MERCURY MULTIPOLE THRUSTER

FIGURE 4

employed were the same as those used by Isaacson and Kaufman<sup>[10]</sup> during their tests with argon and xenon.

The thruster was fitted with a conventional mercury feed system and a hollow cathode. The cathode was a 3 mm dia. tantalum tube with a thoriated tungsten orifice plate having a 0.38 mm dia. orifice. A tantalum foil insert coated with chemical R500 (barium carbonate - strontium carbonate) was located inside the cathode, immediately upstream from the cathode orifice plate. A resistance heater was fixed to the cathode tube adjacent to the tip and the mercury propellant flow rate was controlled to the main propellant plenum and the hollow cathode separately by conventional, sintered tungsten, mercury vaporizers. Compensated high permeance dished grids, having a screen grid open area fraction of 0.67 and an accelerator open area fraction of 0.54, were used. A cold grid spacing of 0.79 mm was maintained with mica spacers. The screen potential was 1000 V while accelerator grid potential was -500 V on all tests. The magnetic baffle assembly shown in Figure 4 was used to control the baffle aperture impedance and hence the primary electron flow into the main discharge region for most of the tests conducted. The need for this magnetic baffle developed however as a result of preliminary tests which deserve some discussion.

Initially the cathode chamber was fitted with a simple mechanical, non-magnetic baffle similar to the one used on SERT II to isolate the cathode chamber plasma from the main discharge plasma. With this baffle installed and with the baffle aperture positioned in the upstream end of the discharge chamber it was observed that a disproportionately large fraction of the ionization was taking place in a very small region near the innermost anode at the upstream end of the discharge chamber, and as a

result performance was poor. The cathode chamber housing was subsequently extended downstream so primary electrons would be injected into a region where they would not be immediately captured by the magnetic fringe field from the inner pole piece and drawn to the innermost anode. In this configuration it was discovered however that the impedance in the baffle aperture could not be adjusted to effect proper primary electron production and injection into the main discharge chamber. With a range of cathode flow rates and aperture areas between the mechanical baffle and the sliding chamber housing (Figure 4), it was found that the potential drop across which primary electron acceleration is accomplished would occur either at the cathode itself or at the magnetic fields protecting the anodes. In either case poor performance was the result. The magnetic baffle shown in Figure 4 was designed and tested (APPENDIX A) and it was found to provide the necessary control on primary electron production. It was installed in a cathode chamber which could be moved axially during thruster operation by means of a stainless steel sleeve which fit inside the innermost pole piece. With this configuration, aperture impedance and the point of electron injection would be varied independently during thruster operation.

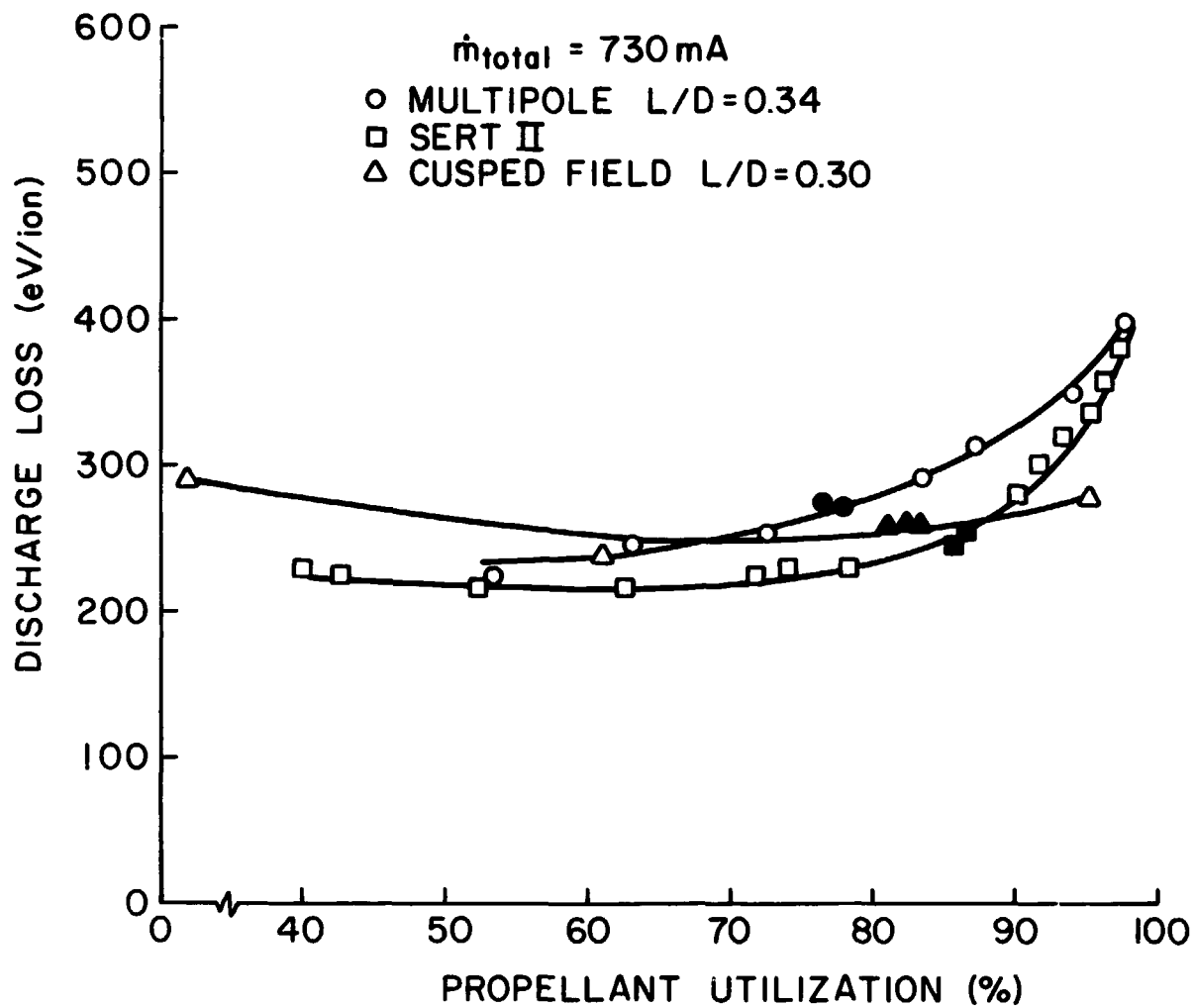
With the magnetic baffle installed, the thruster was operated with 1, 2, 3, and 4 side wall sections and the cathode chamber was extended to the grids or a point 5 cm into the discharge region, whichever was less, with each of these configurations. Total propellant flow was kept to within 1 per cent of 730 mA while data was being taken. Cathode flow rate was adjusted over the range of 3.8 to 8.5 per cent of the total flow to maintain the discharge voltage near 37 V and to facilitate stable operation. Tests were conducted in a 1.2 m dia. by 4.6 m long vacuum facility and

pressures were in the high  $10^{-6}$  torr range during data collection.

Plasma properties were measured using a Langmuir probe which could be moved around inside the discharge chamber. Analysis of the probe characteristics was accomplished using the computer program developed by Beattie.<sup>[11]</sup> Beam data were gathered using an articulated  $\bar{E} \times \bar{B}$  momentum analyzer<sup>[8]</sup> located 68 cm downstream from the grids. The power supplies and instrumentation were connected to the thruster in the manner shown in Reference [12] except for an alteration which allowed the current to each of the anodes of Figure 4 to be measured separately.

### Results

Thruster Length - In the course of optimizing thruster performance it was found that a thruster two side wall sections in length gave the lowest discharge loss and the highest utilization of the configurations tested. The curve obtained with this optimized configuration is shown in Figure 5 along with curves obtained with the SERT II and CMF thrusters operating at the same flow rate and a 37 V discharge voltage (at the solid symbol data points). All thrusters employed the same grids and operated at the same high voltage conditions. These data have not been corrected for double ions because double ion data were not collected at each operating point shown in the figure. It is observed that performance of the three units is similar, with the multipole thruster discharge loss being approximately 50 eV/ion higher than that of SERT II at a utilization near 85%. Comparison of the performance curves obtained as a function of thruster length with the multipole design suggests that somewhat better performance could be obtained if side sections having shorter length increments had been used, but this potential for improvement is considered to be small.

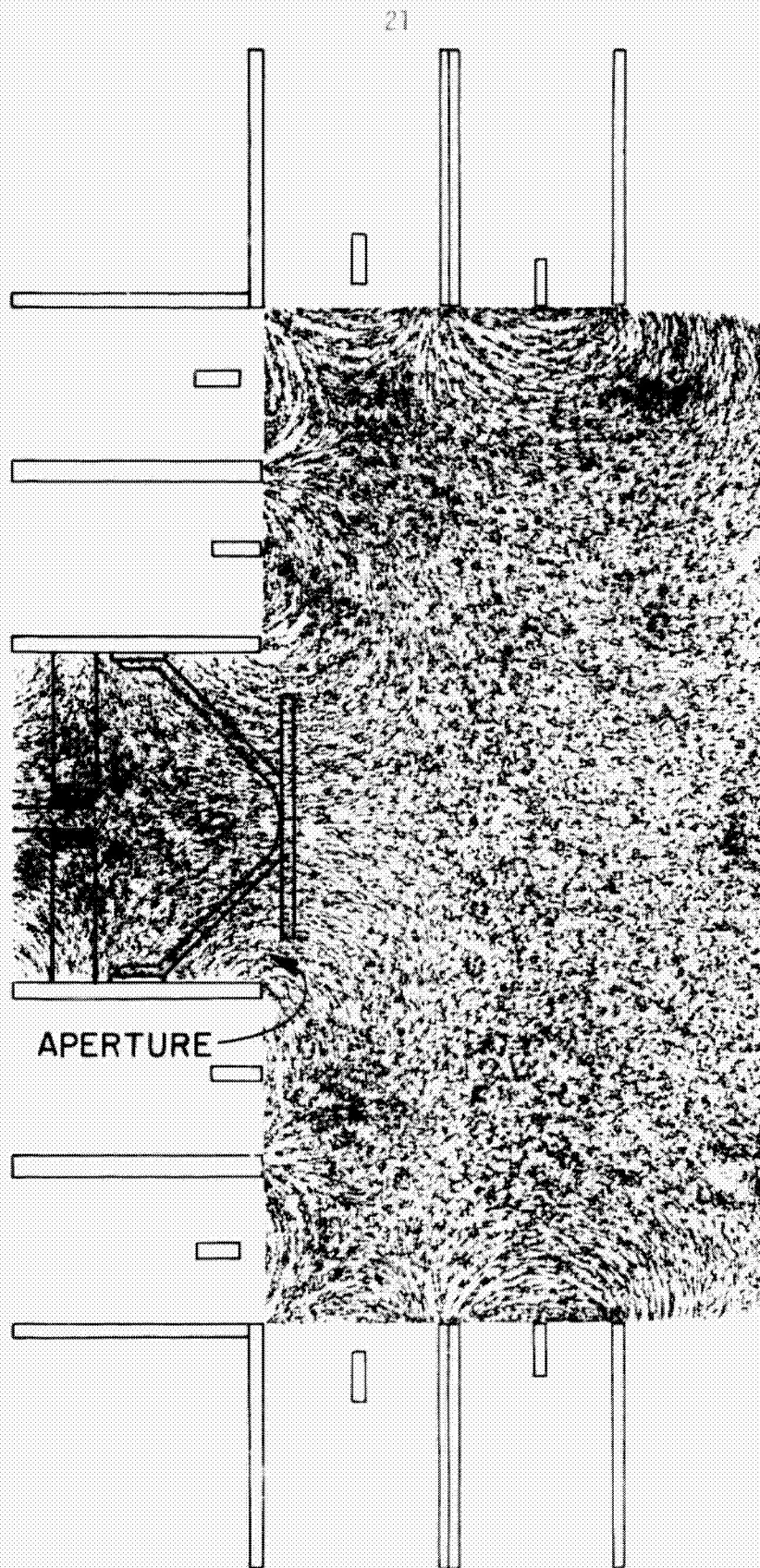


DISCHARGE CHAMBER PERFORMANCE COMPARISON

FIGURE 5

Cathode Location - With a simple, non-magnetic, mechanical baffle installed in the thruster the most notable effect of moving the cathode chamber downstream of pole piece at the upstream end of the thruster was a substantial drop in discharge voltage. This may be explained by considering the effects of the magnetic fringe fields in the baffle aperture region associated with cathode chamber motion. Figure 6 shows the iron filings map of the magnetic field in a thruster having two side wall sections and the non-magnetic baffle assembly. This figure shows that electrons leaving the cathode chamber through the baffle aperture must cross magnetic field lines. Because the magnetic field lines are perpendicular to the direction of electron flow, the magnetic field provides an impedance across which the potential difference responsible for accelerating the electrons to primary electron energies is sustained. Figure 7 shows that same magnetic field with the cathode chamber moved 2 cm downstream. With the cathode assembly in this location not only is the magnetic field in the vicinity of the aperture weaker in intensity, but the field lines lie largely in the same direction as the electron current. Impedance due to the magnetic field is thus virtually eliminated, and control of the baffle impedance at the proper value becomes essentially impossible.

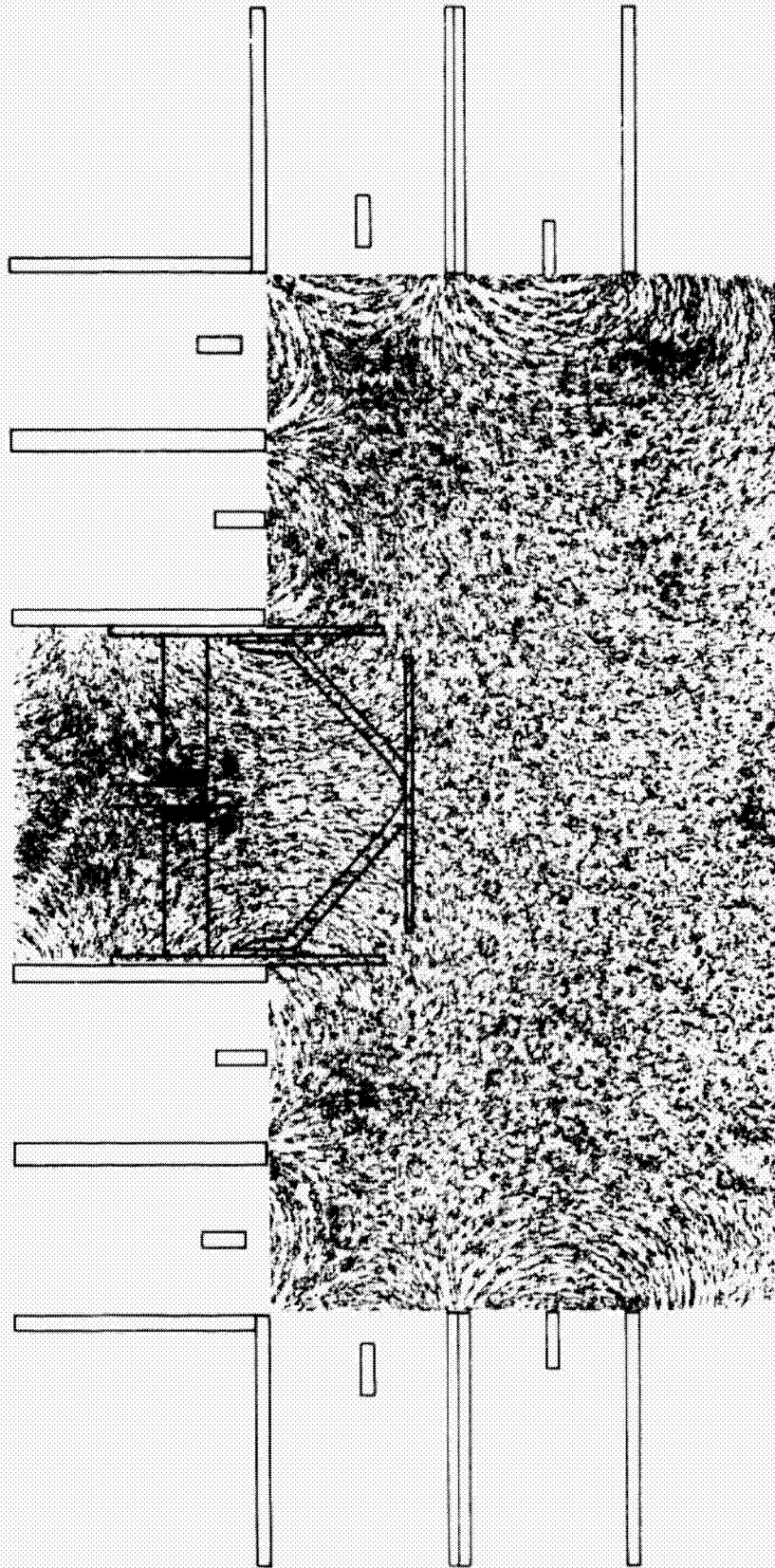
Figure 8 shows the magnetic field configuration in the discharge chamber equipped with the magnetic baffle. The upper half of this figure shows the magnetic field configuration with the cathode aperture flush with the pole piece and the lower half of the figure is the iron filings map obtained with a cathode chamber extension of 3.8 cm. The major effect of the magnetic baffle on the magnetic field within the main discharge chamber occurs at the baffle aperture where the field now tends to be perpendicular to the direction of electron flow for both cathode region positions. With



IRON FILINGS MAP-UPSTREAM NON-MAGNETIC BAFFLE ASSEMBLY

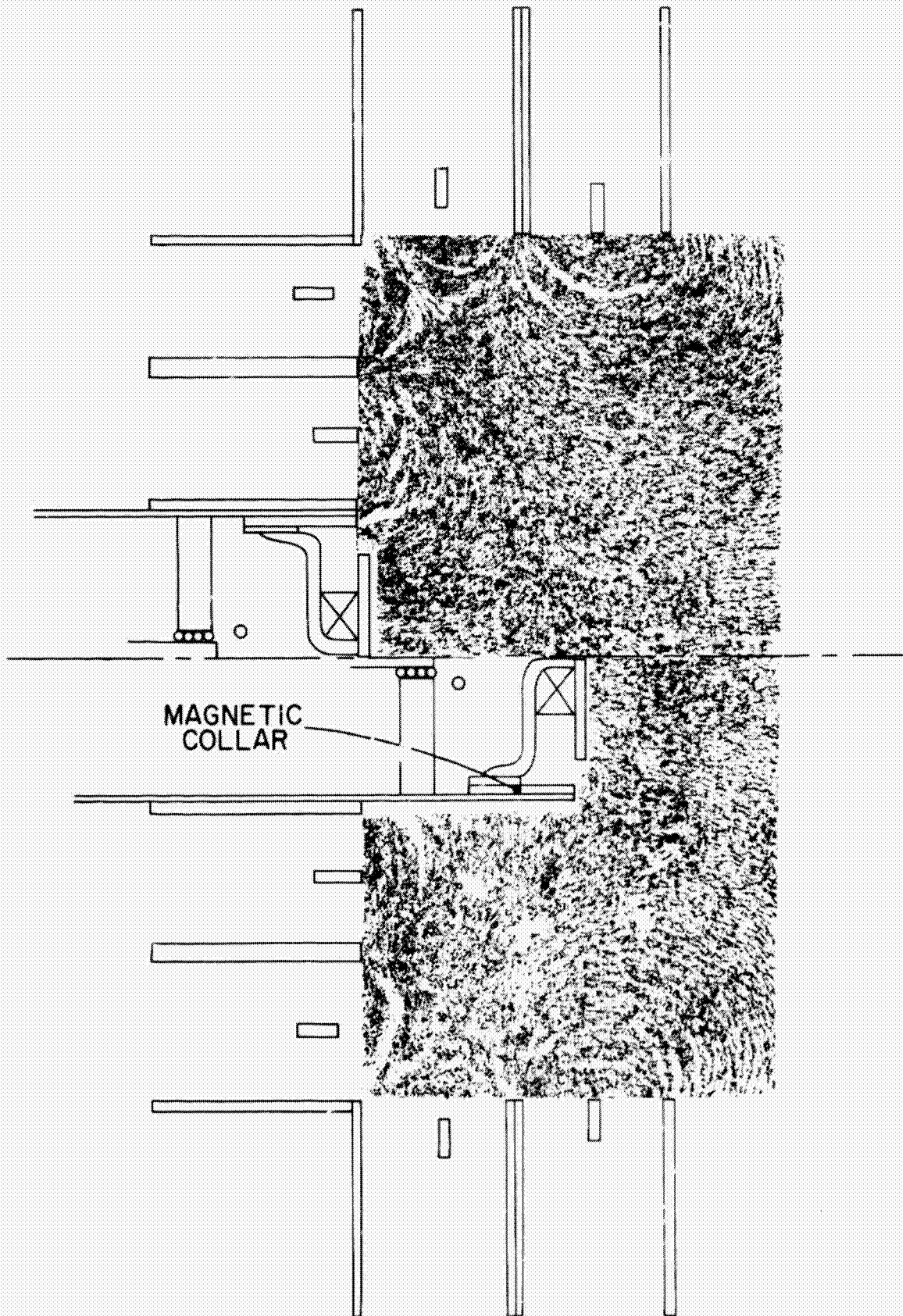
FIGURE 6

22



IRON FILINGS MAP-DOWNSTREAM NON-MAGNETIC BAFFLE ASSEMBLY

FIGURE 7



IRON FILINGS MAP-COMPOSITE MAGNETIC BAFFLE ASSEMBLY

FIGURE 8

the cathode chamber extended as in the lower half of Figure 8 the field shape differs slightly from that observed in Figure 7 in that the field near the innermost pole piece appears to be somewhat more widely dispersed, and field lines tend to go directly into the side of the cathode chamber where the magnetic collar is located.

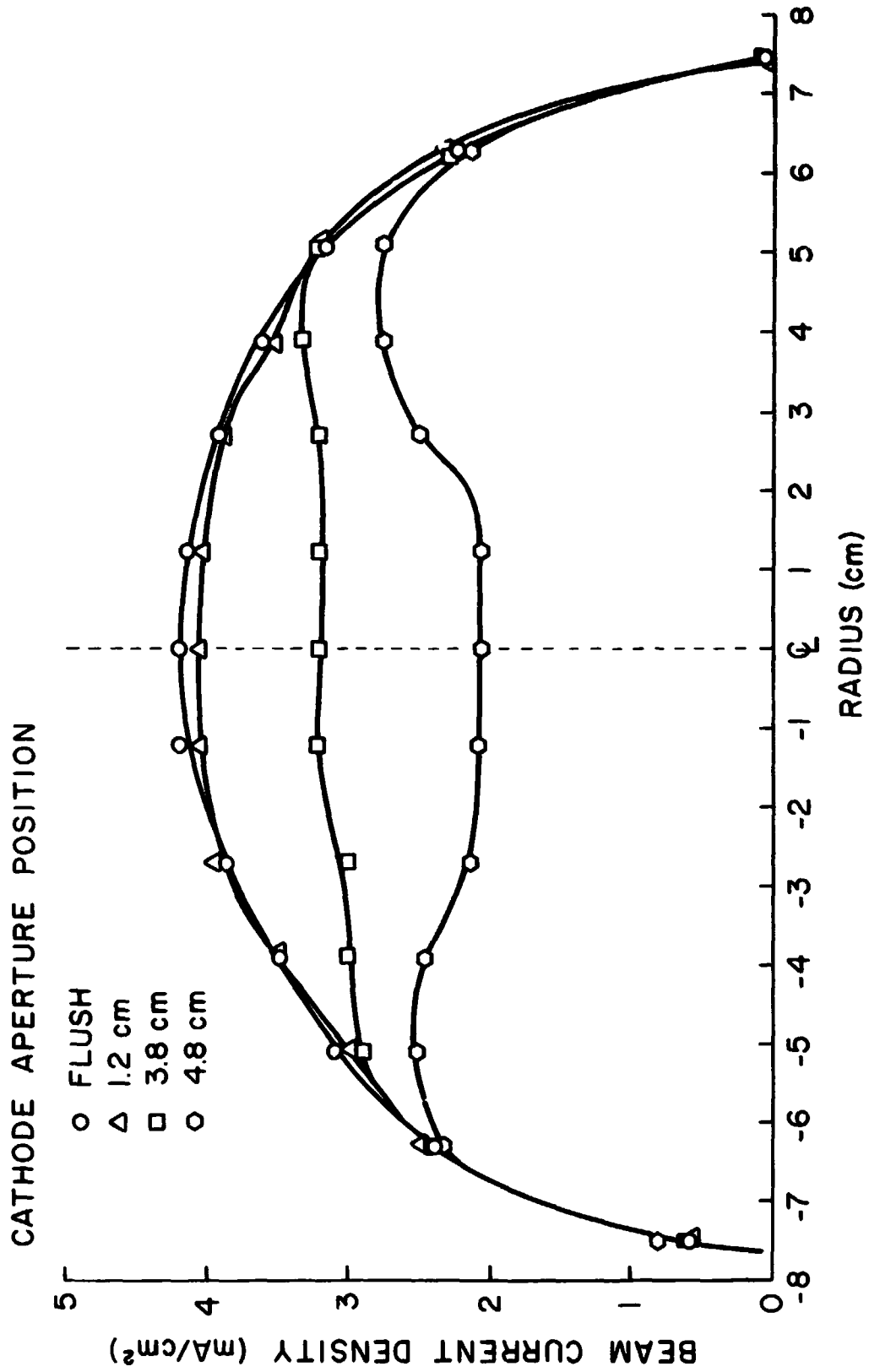
When the magnetic baffle was installed and positioned flush with the innermost pole piece, it required little or no baffle magnet current to effect efficient thruster operation. As the cathode chamber was extended farther and farther into the discharge chamber, away from the innermost pole piece, however the baffle magnet current, required to maintain the desired discharge voltage and an efficient thruster operating condition, increased. These experiments demonstrated that the magnetic field is required across the baffle aperture to effect the voltage drop across which primary electron acceleration is achieved. When electron injection is to be accomplished at a point in the discharge chamber where magnetic field lines do not cross the electron flow path, a magnetic baffle is required to achieve proper operation. Once the proper aperture impedance was established it was found that the point of electron injection into the main discharge chamber did not influence discharge loss and utilization levels substantially unless the injection occurred on magnetic field lines which prevented uniform distribution of the electrons throughout the chamber. Putting the cathode assembly far downstream did however degrade performance slightly because the cathode assembly 1) displaced some volume in which ionizing reactions could have otherwise taken place and 2) provided additional surface on which recombination could occur. Plasma property data taken with the cathode assembly extended confirm the local depletion of ion densities caused by these phenomena.

Cathode aperture location does have an effect on the ion beam profile. Figure 9 shows for example how the ion beam profile is altered as the cathode chamber is moved downstream into the discharge chamber of a thruster that is two side sections long. Cathode chamber extensions of up to 1.2 cm are seen to have little effect on the beam profile, but a 3.8 cm extension results in a flattening of the ion beam profile (flatness parameter of 0.71). Further extensions result in a dip in current density on the beam centerline. These reductions in current density are caused by the reduction in ion density mentioned in the preceding paragraph.

Figure 10 presents a comparison of ion beam profiles obtained with the multipole thruster to those measured in the cusped magnetic field and SERT II thrusters operating at conditions defined by the solid symbols of Figure 5. The flatness parameter corresponding to each curve is identified by the symbol "F" and "L/D" is the length-to-diameter ratio of the thruster. Length as used here is the distance between the grid plane and upstream pole piece faces (cathode pole piece face for SERT II). The lower current densities shown for the multipole thruster reflect the lower propellant utilization obtained with this design. Although the 3.8 cm cathode extension results in the flatter ion beam profile of the multipole configurations it is not preferred because it results in a 3% loss in propellant utilization over that obtained with the flush configuration.

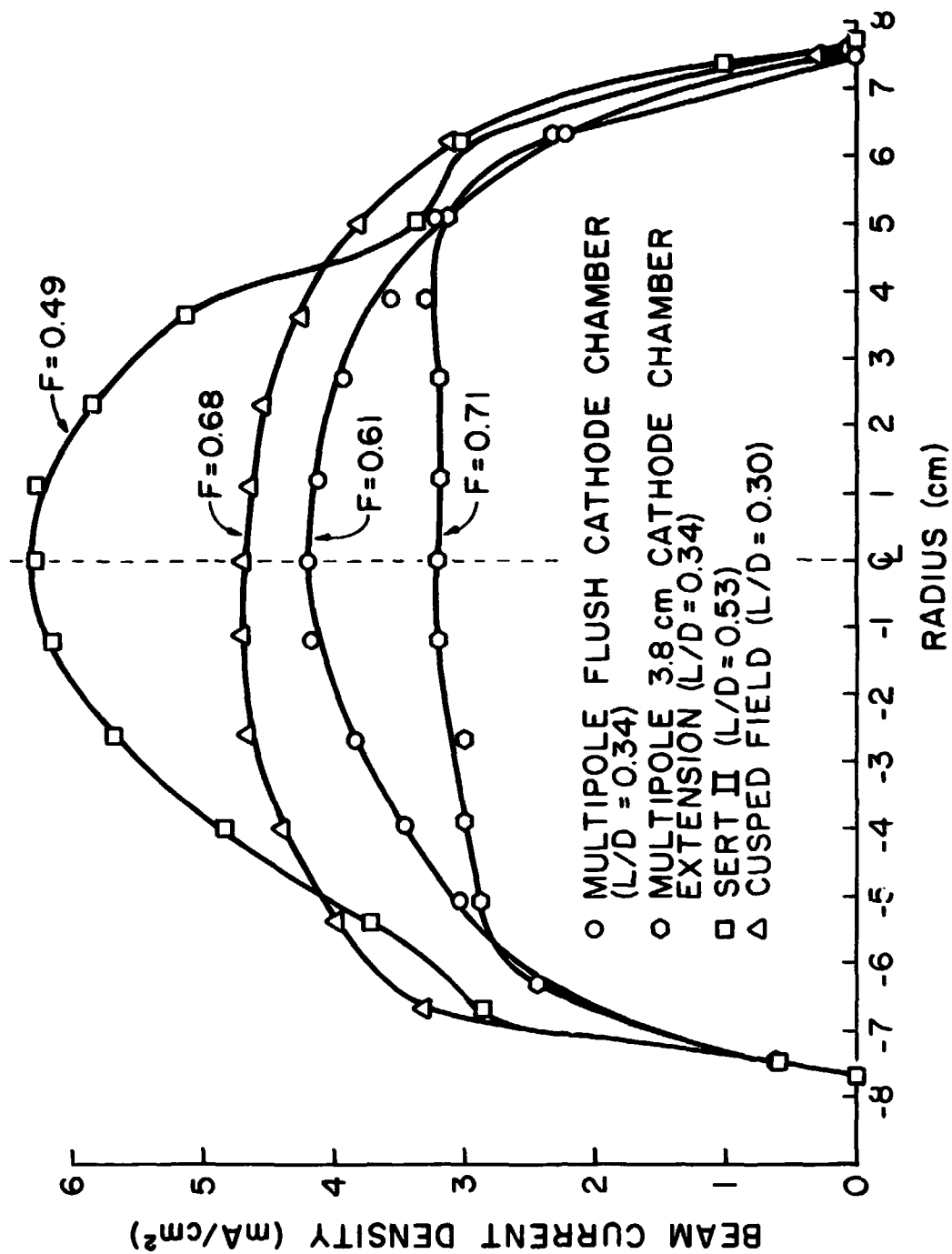
#### Discharge Current Distribution

The distribution of the discharge current between the anodes in the multipole thruster is controlled by the depth and intensity of magnetic fields shielding the anodes and by electron density distributions within the discharge chamber. Figure 11 shows how current drawn to each of the



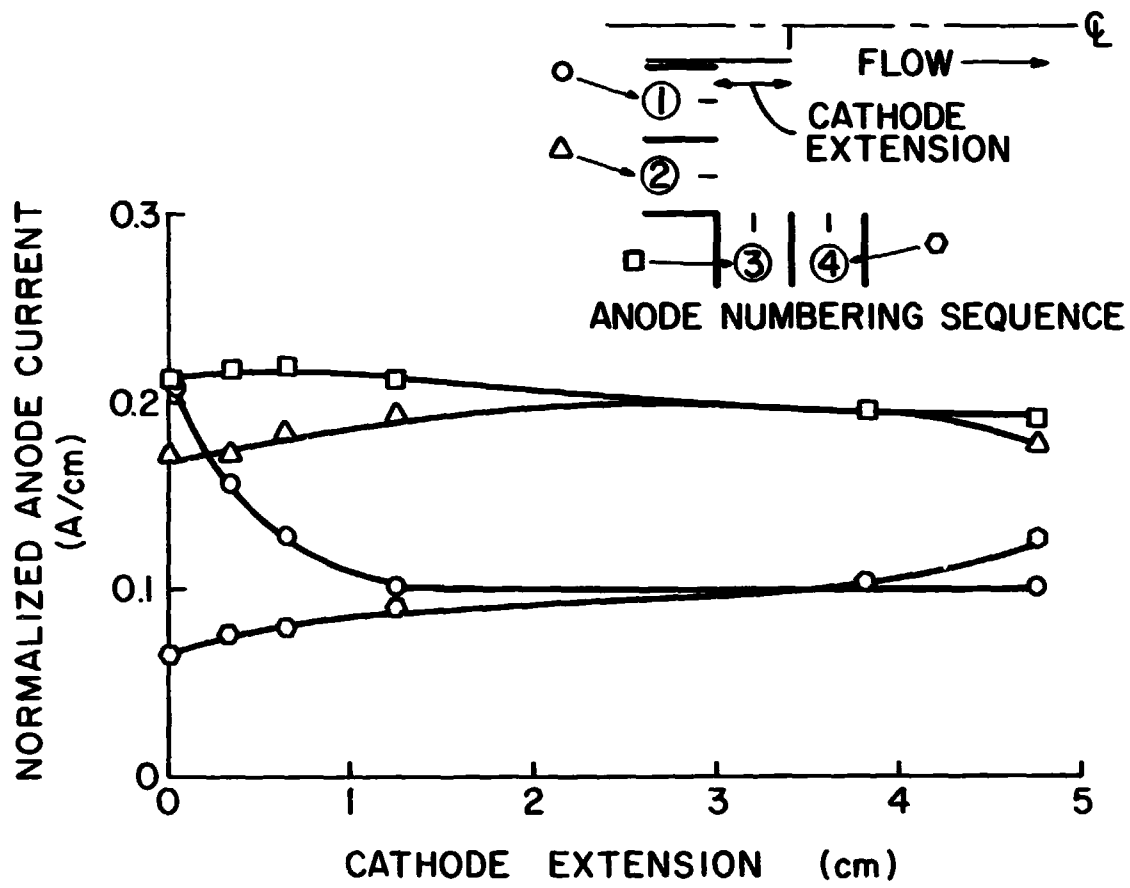
EFFECT OF CATHODE APERTURE LOCATION ON  
ION BEAM PROFILE (MULTIPOLE THRUSTER)

FIGURE 9



ION BEAM PROFILE COMPARISON

FIGURE 10



CURRENT DISTRIBUTION TO ANODES

FIGURE 11

four anodes of the optimized design varies with the position of the cathode chamber. The ordinate of Figure 11 represents measured current drawn by a given anode divided by the radius of that anode. All anodes have the same face width presented to the plasma, so dividing anode current by the radius of the anode in question yields a number representative of the discharge current density at that anode. Anode numbering begins with the anode closest to the cathode chamber and proceeds around the chamber periphery (Figure 11 inset).

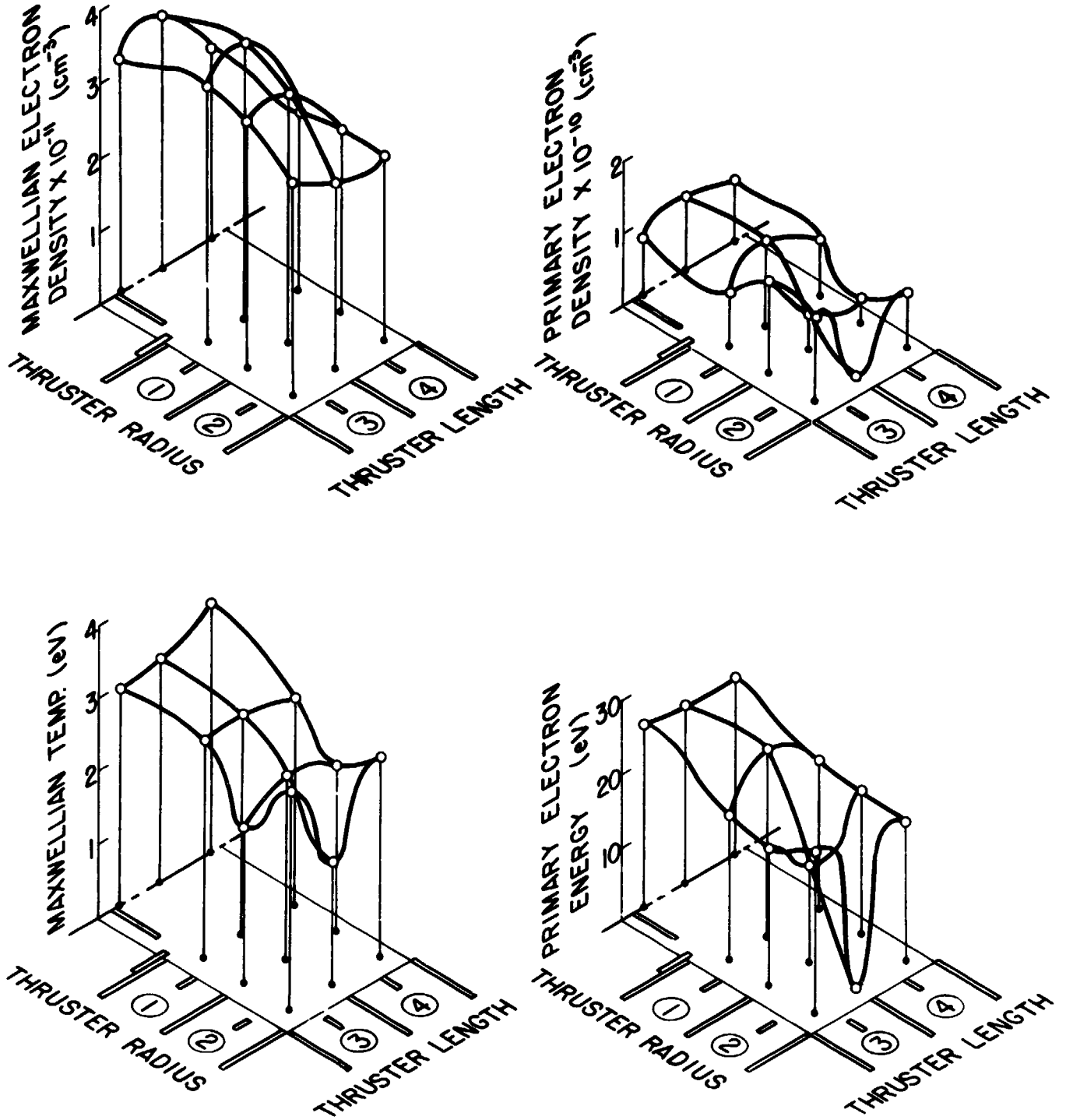
The number one anode is most strongly influenced by the location of the cathode aperture (cathode extension). When the aperture is flush with the upstream pole pieces some of the electrons are injected within the fringe field which protects this anode (see Figure 8). Their path to the anode is thus more direct than it is when electrons are injected into the center of the chamber and they must traverse more magnetic flux to reach the anode. Anodes 2 and 3 are nearly unaffected by cathode location and they both draw essentially the same current density. The slight rise in the current to anodes 2, 3 and 4 is required to compensate for the corresponding drop in current to anode 1 as the cathode chamber is moved forward and sum of current to all anodes is held constant. The downstream anode was found to have much lower currents than other side wall anodes for all thruster configurations tested. This occurs because the conductivity of the plasma across a magnetic field is inversely proportional to  $\int \vec{B} \times \vec{ds}$ <sup>[10]</sup> and this quantity is greater for the downstream anode. This is a result of the greater depth of magnetic field penetration into the main discharge region for the downstream section (a condition which can be seen for the four anode configuration in Figures 6 to 8). Hence even though the total

magnetic flux between the pole pieces of the downstream section is the same as that between other sections, the integral is greater because more flux lines lie interior to that anode and they are more dispersed. Consequently, less current is conducted. It should be noted that the decline in the current to anode 1 is also partially due to the same effect. This decline with cathode chamber extension was observed on all thruster configurations tested. As previously noted and shown in Figure 8 the fringe field in the vicinity of anode 1 becomes somewhat more widely dispersed as the cathode chamber is extended. The impedance between this anode and the plasma is thereby increased, and anode current goes down.

It is believed that further improvements in performance could be realized if magnetic fields and/or anode positions were adjusted so equal current densities were drawn to each anode but this optimization has not been carried out.

Discharge Stability - Discharge current oscillations tended to occur in the multipole thruster at higher values of main and/or baffle magnet currents. Good performance was generally realized at the threshold of these oscillations and this frequently made thruster operation difficult. Although the amplitude of discharge oscillations was influenced by both magnet currents, it was most sensitive to main magnet current. Since these oscillations were not reported by Isaacson and Kaufman<sup>[10]</sup>, their presence here is presumed to be related to the hollow cathode chamber.

Plasma Properties - The results of Langmuir probe measurements in the two side wall section multipole configuration with the cathode chamber extended 3 mm are shown in Figure 12. Toward the center of the discharge chamber the plasma properties are observed to be well-behaved and fairly



MERCURY MULTIPOLE PLASMA PROPERTIES

FIGURE 12

uniform. Toward the sidewalls, however, there are strong perturbations due probably to the influences of the magnetic fields and anodes there. Note that near the pole piece between anodes 3 and 4 primary electrons appear to vanish, whereas near the adjacent anodes the values for primary electron density and energy are higher. A similar though less pronounced effect on primary energy appears near the pole piece between anodes 1 and 2. Maxwellian temperature is also depressed at those same locations. Compared to the SERT II and Cusped Field Thrusters the mean Maxwellian electron density is high and the mean temperature is low in the multipole thruster. Beattie's study<sup>[2]</sup> of the effect of anode-critical field line separation distance on plasma properties and thruster performance, suggests the multipole magnetic field should be increased or anodes 2 and 3 should be recessed more to increase electron temperature and improve performance. Unfortunately increases in magnetic field intensity were precluded during these tests by the onset of instabilities.

Visual observation of the thruster during operation revealed regions of relatively intense luminosity near the pole pieces between anodes 1 and 2 and anodes 3 and 4. The dip in Maxwellian temperature and primary electron energy at these same locations suggests they may be regions of high collision frequency. Such regions of high collision frequency at the thruster periphery would explain the increase in beam current density observed by Robinson<sup>[13]</sup> at the edge of a 30 cm diameter multipole gas thruster.

#### Doubly Charged Ions

Operating conditions and performance data obtained with optimized multipole and cusped magnetic field thrusters are listed in Table IV along

with similar information for the SERT II thruster. The bulk of the data presented here simply represents a retabulation of data presented previously, but the doubly charged ion data in the last two rows are new. These data show the doubly charged ion current ratio and the flatness parameter for the doubly charged ions are both intermediate between values observed for the SERT II and the cusped field thrusters. It was observed also that inserting the cathode chamber downstream to the 3.8 cm location reduced the doubly charged ion content of the ion beam substantially. This suggests that structure, such as a cathode chamber, extended close to the grids, while it degrades performance, also reduces the centerline doubly charged ion density substantially.

Table IV  
Comparison of Mercury Thruster Performance

<u>Hardware</u>			
Thruster	Multipole	SERT II	Cusped Field
Length-to-Diameter Ratio	0.34	0.53	0.30
<u>Operating Conditions</u>			
Screen (accel) Potential (kV)	1.0 (.5)	1.0 (.5)	1.0 (.5)
Propellant Flow (mA)	730	725	730
Discharge Current (A)	4.0	4.06	4.3
Discharge Voltage (V)	36.6	37.5	36.7
<u>Performance Data</u>			
Beam Current (mA)	548	654	625
Discharge Loss (eV/ion)	283	239	256
Propellant Utilization	0.73	0.87	0.84
Beam Flatness	0.61	0.49	6.68
Doubly-to-Singly charged ion current ratio	0.064	0.081	0.052
Doubly charged ion Beam Flatness	0.34	0.27	0.33

### Conclusions

Optimization of the length of a 15 cm diameter mercury multipole thruster has shown that the best performance is realized in the vicinity of a length-to-diameter ratio of 0.34. Although further improvements in multipole thruster performance might be expected if the length of the side sections which determine the optimization length intervals were adjusted and if magnetic field or anode position adjustments were made to insure equal discharge current density levels to each anode, the discharge loss and propellant utilization levels are comparable to those observed on the cusped field and SERT II thrusters.

Proper thruster operation requires the use of a magnetic baffle and the preferred point of electron injection is at the upstream end of the discharge chamber. Moving the point of electron injection downstream reduces the ion density on the thruster centerline and this reduces propellant utilization slightly but it also increases the ion beam flatness and reduces the doubly charged ion density on the thruster centerline. Doubly-to-singly charged ion current ratios and ion beam flatness for the multipole with upstream electron injection are better than those observed in SERT II and poorer than observed in the cusped field thruster. The multipole thruster operates less stably than the other two thrusters.

## ION OPTICS STUDY

Graeme Aston

The bulk of the work conducted on this study during the grant period has been reported previously<sup>[14]</sup> and this information will not be repeated here. This previous work has shown that, to a good approximation, complete independence may be assumed to exist between the effect each geometrical grid parameter has on ion beam divergence. These results were however obtained for a total accelerating voltage ( $V_t$ ) of 600 volts and an ion source discharge voltage ( $V_D$ ) of 40 volts. In general, broad beam ion sources may operate over a wide range of accelerating and discharge voltages. Ion beam divergence characteristics for two-grid multiple-aperture accelerator systems were therefore investigated for total accelerating voltage and discharge voltage variations.

### Parameter Definitions

The following grid geometry definitions are used:

- $l_g$  = grid separation distance
- $d_s$  = diameter of screen apertures
- $d_a$  = diameter of accelerator apertures
- $t_s$  = thickness of screen grid
- $t_a$  = thickness of accelerator grid
- $l_e$  = effective acceleration length<sup>[15]</sup>.

### Apparatus and Procedure

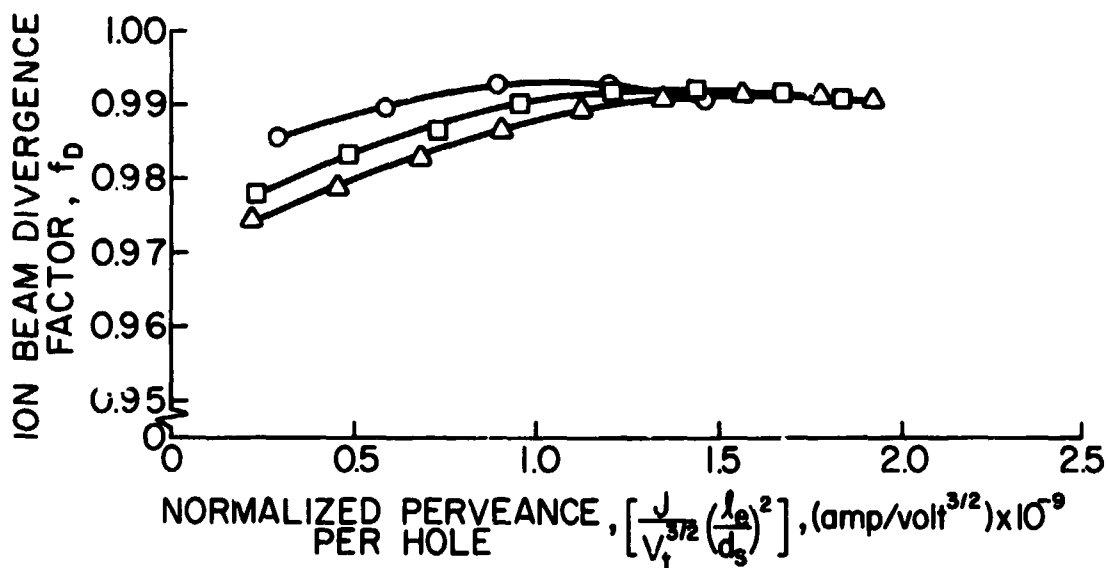
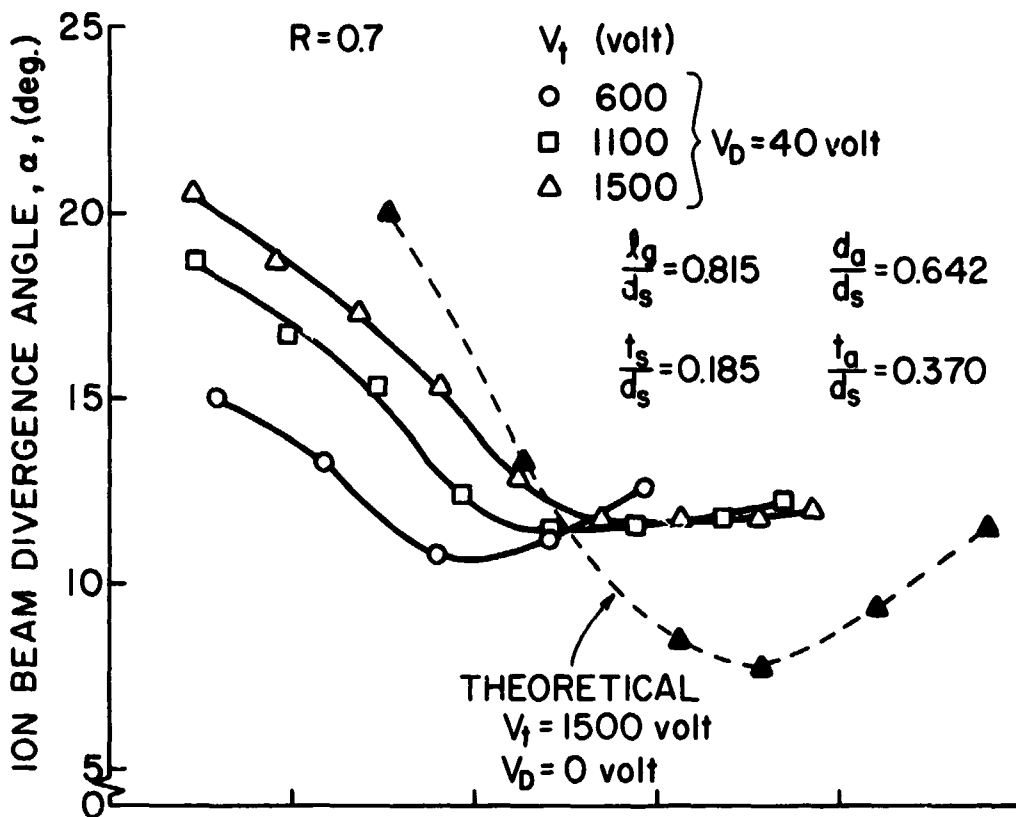
Sheet carbon grid sets, employing a nineteen hole hexagonal array, were operated over a wide range of total accelerating and discharge voltages. At each voltage condition the beam current,  $J$ , was increased up to the

maximum beam current obtainable for that grid set. This limit was characterized by excessive accelerator grid impingement current accompanied by no further beam current increases. Ion beam divergence angle ( $\alpha$ ) and ion beam divergence factor ( $f_D$ ) variations were determined at several beam currents up to this maximum value. Reference [14] details ion source construction and operation, as well as the beam profile analysis method employed.

### Results and Discussion

Figure 13 shows the variation of ion beam divergence curves as the total accelerating voltage ( $V_t$ ) is increased with constant discharge voltage ( $V_D$ ) at a constant net-to-total accelerating voltage ratio ( $R$ ) of 0.7. Geometrical grid parameters were held constant at the values indicated. The minimum ion beam divergence angle and maximum ion beam divergence factor are observed to move to higher values of normalized perveance per hole, as values of the discharge voltage-to-total accelerating voltage ratio are decreased. Qualitatively, the curve shapes are similar. Only a small change in minimum ion beam divergence angle and maximum ion beam divergence factor are observed. A grid set using a reduced grid separation ratio,  $\frac{l_g}{d_e} = 0.494$ , was investigated also, and no change from the trends shown in Figure 13 was apparent. The decreased grid separation ratio merely increased the overall ion beam divergence, resulting in uniformly increased ion beam divergence angles and decreased ion beam divergence factors. This trend was predictable from the preliminary ion-optics study results.<sup>[14]</sup>

Theoretical ion beam divergence angle variation, from Kaufman<sup>[15]</sup>, is shown also in Figure 13. Kaufman's predictions were for a single aperture grid geometry with a total accelerating voltage of 1500 volts and zero discharge voltage and he did not study the effects of varying the discharge



EFFECT OF TOTAL ACCELERATING VOLTAGE

ON ION BEAM DIVERGENCE

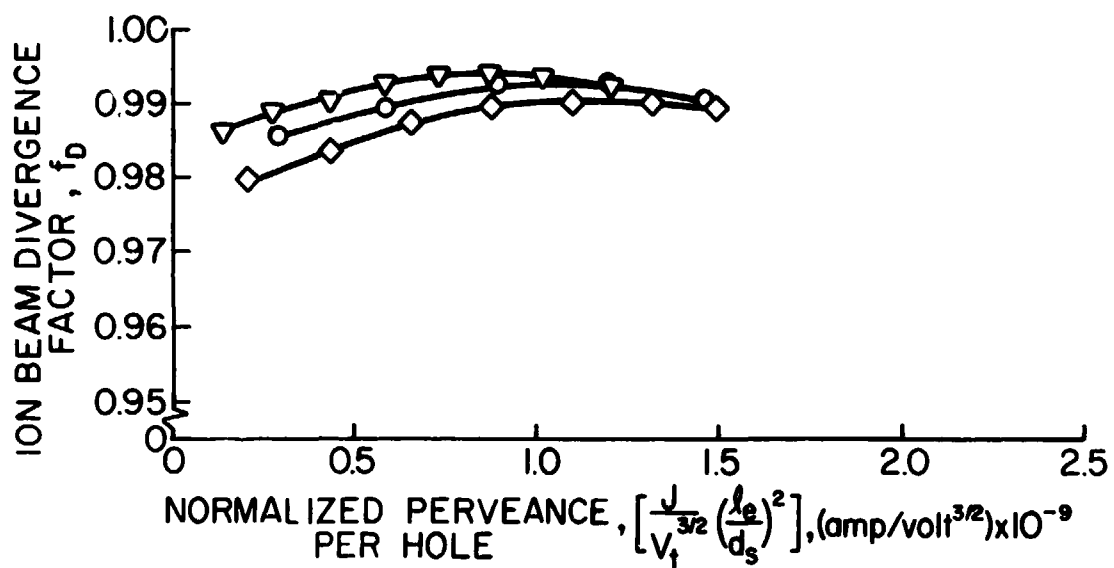
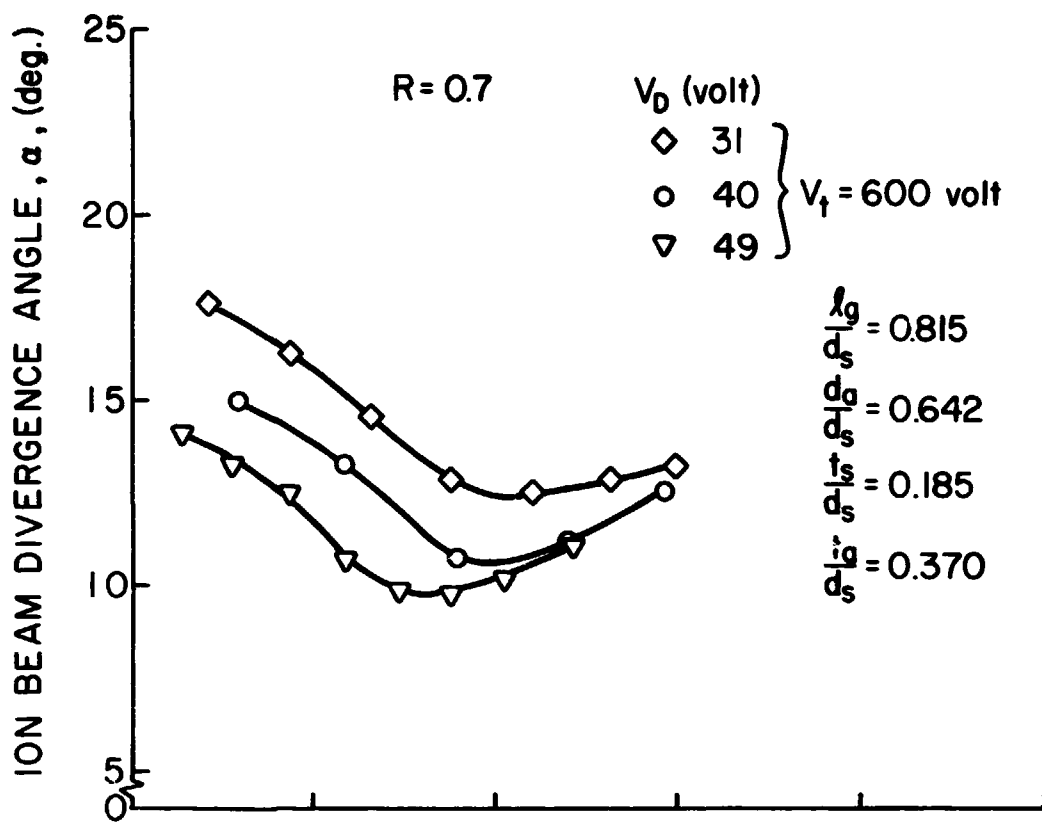
FIGURE 13

voltage-to-total accelerating voltage ratio. Experimentally, as this ratio is decreased, the normalized perveance per hole at which the minimum ion beam divergence angle occurs, approaches that predicted theoretically and closer agreement between theory and experiment is observed. Quantitatively, however, the overall agreement is still poor.

Figure 14 shows the effect of increases in discharge voltage at constant total accelerating voltage on ion beam divergence. The net-to-total accelerating voltage ratio and geometrical grid parameters are unchanged from Figure 13. Increasing ion source discharge voltage significantly reduces ion beam divergence. The minimum ion beam divergence angle is also reduced significantly and the maximum ion beam divergence factor is increased significantly as discharge voltage increases. Also, the minimum ion beam divergence angle and maximum ion beam divergence factor are moved to higher normalized perveance per hole values, as the discharge voltage-to-total accelerating voltage ratio is decreased.

In summary, decreasing the discharge voltage-to-total accelerating voltage ratio moves the minimum ion beam divergence angle and maximum ion beam divergence factor to higher values of normalized perveance per hole. However, the magnitudes of ion beam divergence angle and ion beam divergence factor appear to be strongly dependent on discharge voltage variations alone. Total accelerating voltage variations appear to produce only a second order variation in these quantities.

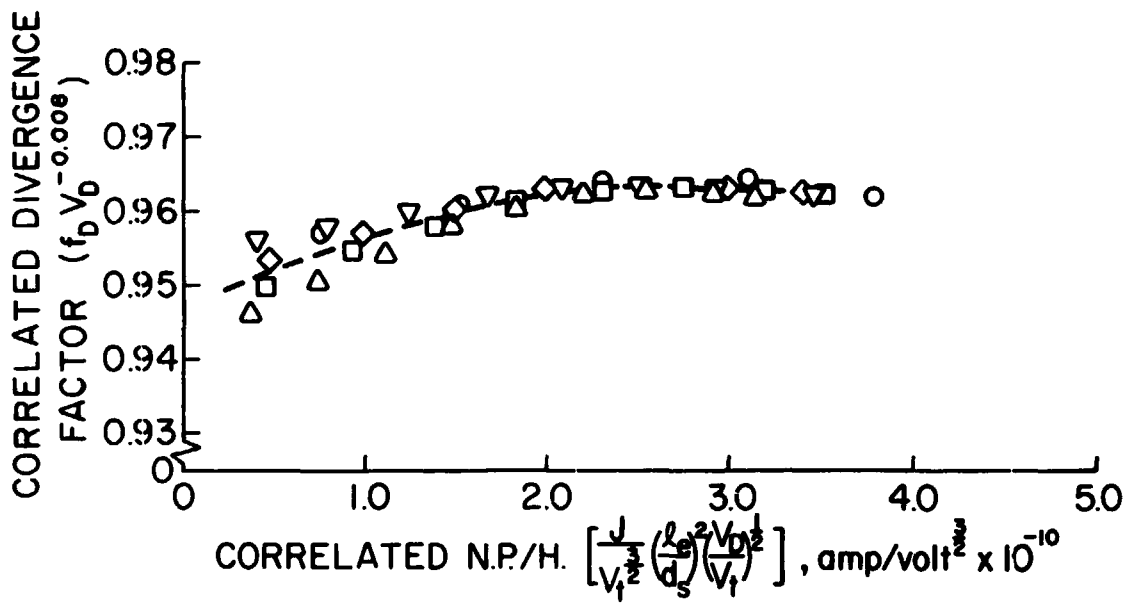
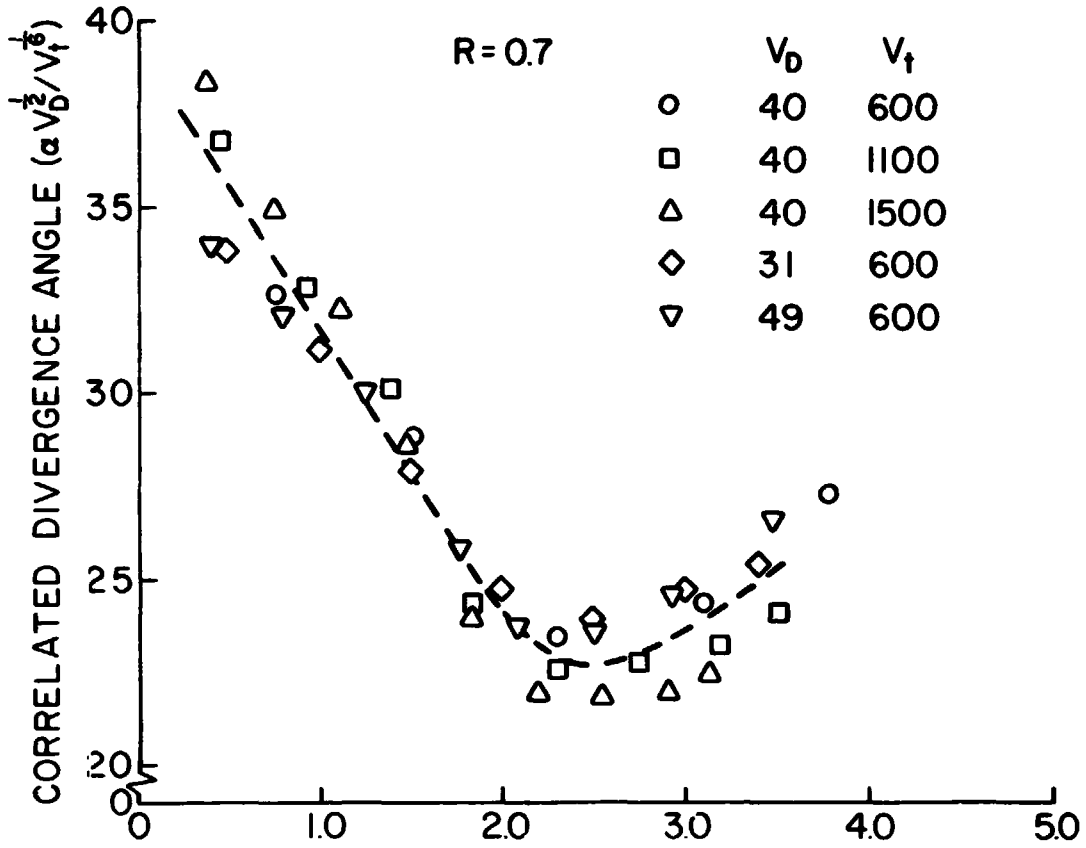
The distinct ion beam divergence trends discussed above suggest correlation parameters that account for these trends may be found. Figure 15 shows how the data of Figures 13 and 14 can be coalesced using appropriate correlating parameters. Variations in normalized perveance



EFFECT OF DISCHARGE VOLTAGE ON

ION BEAM DIVERGENCE

FIGURE 14



VOLTAGE CORRELATED ION BEAM DIVERGENCE CHARACTERISTICS

FIGURE 15

per hole have been correlated using the ratio  $(V_D/V_t)^{1/2}$ . Variations in ion beam divergence angle have been correlated using the ratio  $V_D^{1/2}/V_t^{1/6}$ , while ion beam divergence factor variations have been correlated using the parameter  $V_D^{-0.008}$ . Figure 15 shows that ion beam divergence changes, caused by large discharge voltage and total accelerating voltage variations, may be correlated fairly successfully using these parameters.

Physically, the processes which permit the correlation parameters of Figure 15 to apply are difficult to understand. The screen hole plasma sheath position and shape must vary with discharge voltage and total accelerating voltage changes. However, without means of actually observing the screen hole plasma sheath, its varying position and shape is difficult to infer. Further work into the physical significance of these correlating parameters needs to be done.

### Conclusion

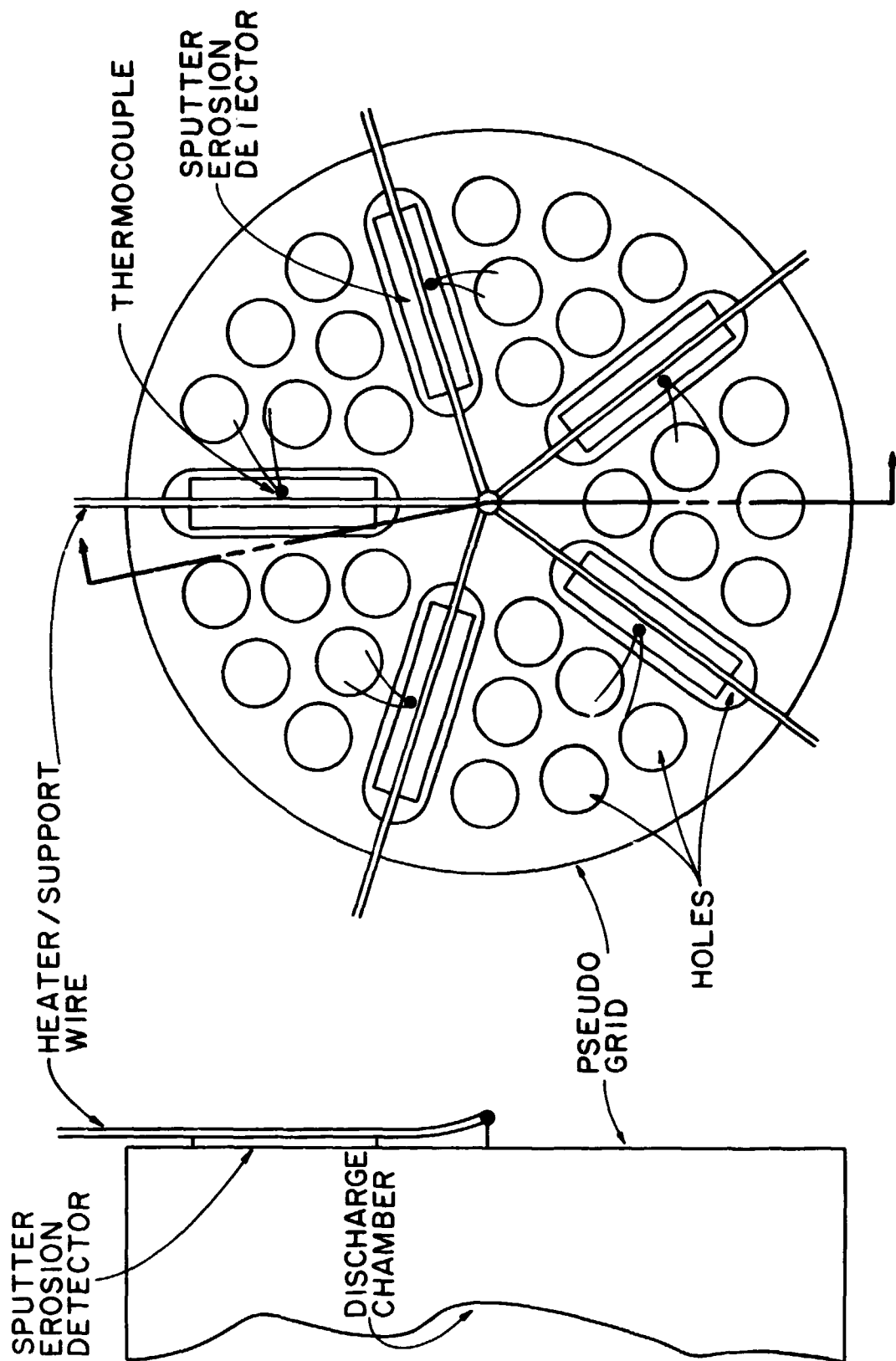
A preliminary investigation has shown variations in discharge voltage and total accelerating voltage strongly affect ion beam divergence. Decreasing the discharge voltage-to-total accelerating voltage ratio moves the minimum ion beam divergence angle and maximum ion beam divergence factor to higher values of normalized perveance per hole. Changes in the magnitudes of ion beam divergence angle and ion beam divergence factor depend primarily on discharge voltage variations alone. Correlation parameters accounting for these trends have been formulated. Further grid set geometries require investigation to refine these correlation parameters.

## EFFECT OF TARGET TEMPERATURE ON SPUTTERING RATE

Tests on mercury ion thrusters have revealed that sputter erosion of discharge chamber components frequently limits the useful lifetime of a thruster.<sup>[9]</sup> One variable which can influence the rate of sputter erosion is the temperature of the surface being subjected to the erosion (target).<sup>[16]</sup> While the sputtering rate of a pure target is independent of its temperature, the surfaces within an ion thruster discharge chamber are continually being struck by relatively small numbers of foreign atoms from other surfaces within the discharge chamber and test facility and by the mercury propellant atoms themselves. These foreign atoms can tend to either protect the surface or enhance erosion, and the extent of the protection or degradation they provide is dependent on the target temperature. The temperature dependence comes about because of its effect on the residence time and migration rate of these impurities on the target surface.<sup>[16, 17]</sup> The purpose of this study has been to evaluate sputtering rates at a function of target temperature in a mercury thruster discharge chamber environment to determine whether or not these impurity atoms play a significant role in either enhancing or retarding the rates of erosion within the discharge chamber.

### Apparatus and Procedure

In order to conduct this test a 15 cm diameter SERT II thruster was equipped with the pseudo grid, shown in Figure 16, in place of the conventional screen and accelerator grid set. This pseudo grid is fitted with five sputter erosion detectors mounted to heater wires and instrumented with thermocouples which sense the sputter erosion detector temperature.



SPUTTER EROSION TEST JIG

FIGURE 16

Because the detectors are located at the same radius and at different azimuthal locations on the axisymmetric discharge chamber each one is exposed to essentially the same discharge plasma. The basic idea of the test was to control the temperatures of each of the erosion detectors at different values over the range from 200° to 500°C, through application of appropriate heater powers, over a sufficient period of time to effect measureable sputter erosion on the erosion detectors. Because the pseudo grid and erosion detectors were maintained at thruster body potential, they were exposed to the same bombarding ion energy as one would expect on a screen grid surface.

In order to monitor the discharge plasma characteristics a Langmuir probe was mounted in the discharge chamber at a radius near the midpoints of the detectors and 1 cm upstream of the pseudo grid. Traces were recorded from this probe at 1/2 hour intervals during the typical several hour test run. Analysis of these traces yielded plasma potentials, temperatures, energies, and densities which were used to determine the average plasma properties over the test duration. These average data were subsequently used as input to the model developed by Peters<sup>[4]</sup> to determine doubly and singly charged mercury ion fluxes to the detectors at a location near their midradii.

In view of the sensitivity of ion sputtering rates to double ion densities and energies and the strong dependence of these properties on thruster discharge voltage and current, it became necessary to control discharge voltage and current precisely. This in turn necessitated the installation of independent main and cathode propellant feed systems and a magnetic baffle. Using these controls the discharge voltage could be

held constant to within  $\pm 1$  volt at a constant discharge current. Tests were conducted in a 1.2 m dia. x 4.6 m long vacuum chamber at a background pressure in the  $10^{-6}$  torr range.

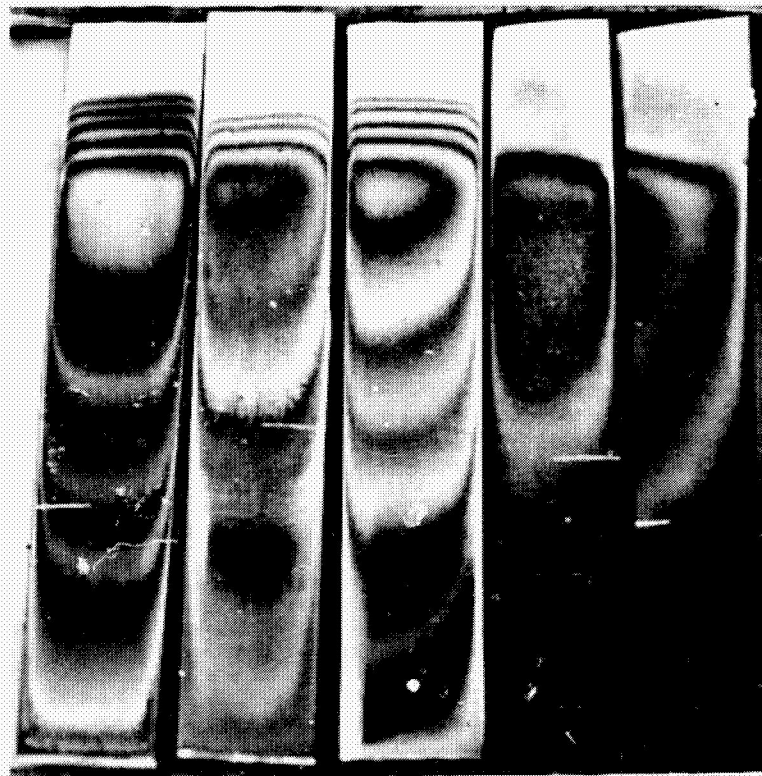
The sputter erosion detectors used for this test were 0.8 cm x 3.8 cm x 0.1 cm thick copper plates silver soldered to the heater wires on one side and coated with the multilayer erosion detector developed by Free<sup>[18]</sup> on the other. These detectors were fabricated with ten layers of the material whose sputter erosion rate was to be measured alternated with ten layers of copper. In order to determine quantitative erosion rates, it was hoped it could be assumed that copper eroded very rapidly compared to the test material so the bulk of the exposure time would be spent in eroding the test material. In the case of this study, detectors were fabricated with alternate  $500\text{\AA}$  (nominal) layers of copper and the test metal involved (either tantalum, molybdenum or 304 stainless steel). After the samples had been exposed to the mercury discharge for the test duration and several layers of the test material and copper had been removed, the samples were removed from the pseudo grid and mounted in a test jig where the remaining layers could be machined off of the detector at its outer edge using an argon ion machining process. Subsequent counting of the layers remaining near the midpoint of the detector enabled one to determine the layers removed during the test at the location where plasma properties were known. From this information the sputtering rate could be estimated.

### Results

Preliminary tests were conducted at a discharge voltage of 55 V where accelerated tests could be conducted and rapid evaluation of trends and testing concepts was possible. During a typical test the Maxwellian electron

temperature was  $13.5 \pm 0.7$  eV, the primary electron energy was  $45.5 \pm 1$  eV, the Maxwellian electron density was  $1.1 \times 10^{11} \pm 0.2 \times 10^{11} \text{ cm}^{-3}$ , the primary electron density was  $1.8 \times 10^{10} \pm 0.2 \times 10^{10} \text{ cm}^{-3}$  and the plasma potential was  $60.8 \pm 0.8$  V. The limits on each of the above quantities define the maximum variation about the mean value as observed in Langmuir probe results recorded throughout the test. Using the mean values cited above in Peters' double ion model,<sup>[4]</sup> a doubly-to-singly charged ion density ratio of 3.7% was calculated. The tantalum/copper sputter erosion detectors removed from the test jig after 6.7 hours of exposure to the plasma defined above are shown in Figure 17. The detectors, as shown, have also been argon ion machined on their upper (greatest radius) edge to expose the base metal and reveal the layers remaining. The radius at which the Langmuir probe was located relative to each detector is indicated approximately by the arrow on the right and exactly by a small scribe mark on each sample.

Examination of Figure 17 shows several anomalies which were typical of the results obtained in these tests with each of the materials investigated. 1) The relative widths of the copper and tantalum layers are nearly equal. This suggests that the assumption of very rapid erosion of copper relative to tantalum is invalid. 2) While the erosion rates observed at 490°C and 420°C are considerably higher than those observed at lower temperatures as one would expect, scatter is apparent in the results (eg. the rate pertaining to the 300°C sample is greater than that observed for the 360°C one). One additional observation not apparent from the photograph of Figure 17 is the difference in physical appearance of the two highest temperature samples. While the low temperature samples appear shiny, the higher temperature samples generally had a velvet-like appearance, and it was considerably more tenacious and resistant to machining by a 500 eV argon ion beam.



} LOCATION OF  
LAYER REMOVAL  
TO BASE METAL  
(500 eV ARGON  
ION MACHINED)

← LANGMUIR  
PROBE  
RADIUS

↑ 360°C    ↑ 300°C    ↑ 200°C    ↑ 490°C    ↑ 420°C

} NOMINAL  
TEST  
TEMPERATURE

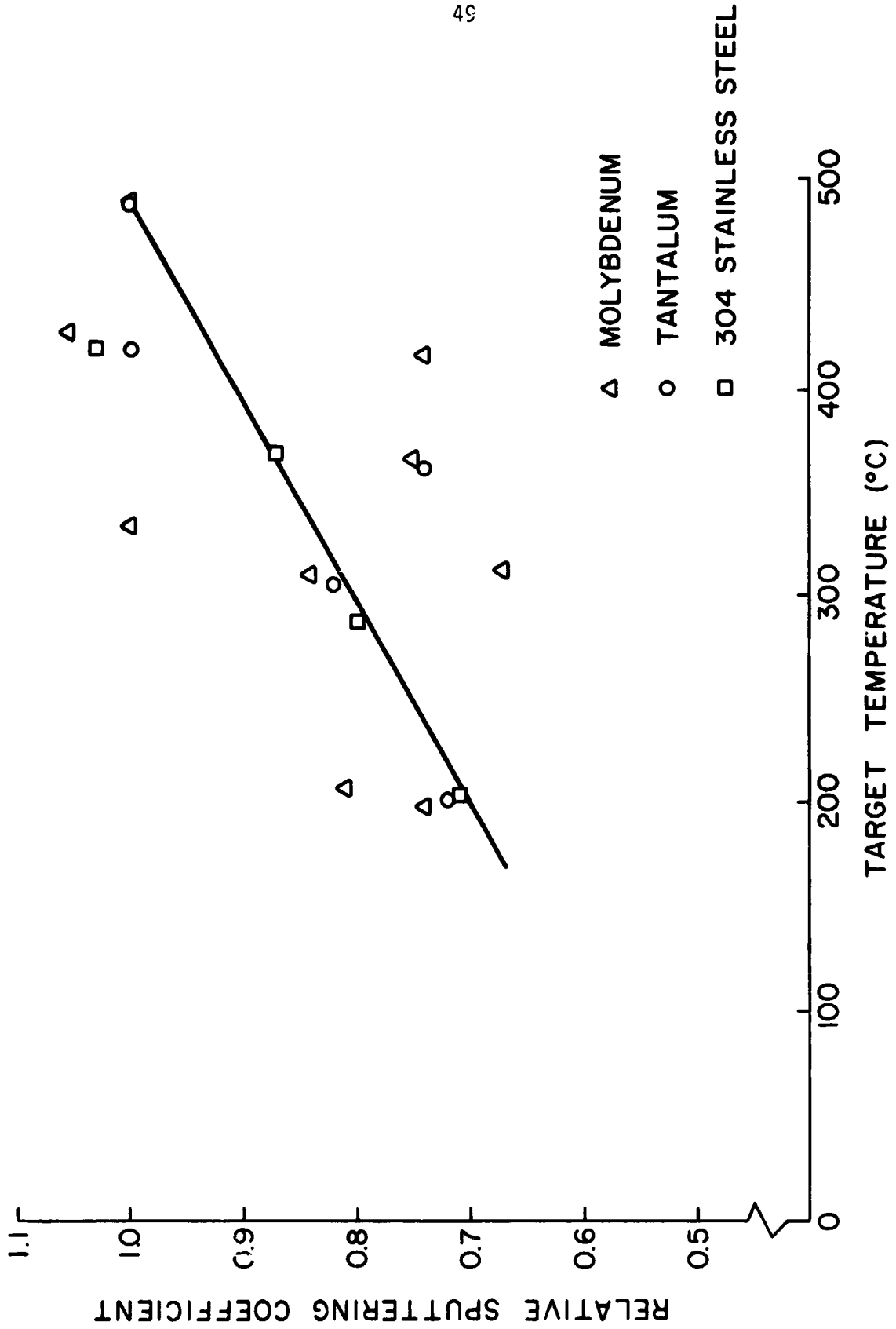
TANTALUM/COPPER EROSION DETECTORS

FIGURE 17

On the basis of the relative widths of the copper and tantalum bands in Figure 17 it appears both materials erode at about the same rates when they are layered in the manner described. Assuming this is valid one can determine erosion rates for each of the detectors in Figure 17. If these rates are then normalized by dividing by the sputtering rate of the highest temperature detector and the resulting normalized sputtering rates are plotted against target temperature, along with similar results obtained from tests using other test materials, the results of Figure 18 are obtained. This figure suggests that indeed the erosion rate of the detectors does increase with temperature although there is considerable scatter in the results. This scatter might be attributed to variations in the plasma properties within the discharge chamber, or variations in the properties or thicknesses of the erosion detector layers, but it is significantly greater than that due to the inherent limit in precision imposed by the ratio of layer thickness to total thickness eroded in a test.

#### Discussion and Conclusions

While the erosion rate of the erosion detectors does appear to increase with temperature the extrapolation from this observation to a conclusion that the same thing will happen with pure test metal probably cannot be made. This statement is made in light of recently discovered studies by Wehner<sup>[17]</sup> which suggest that the phenomenon referred to as cone formation is probably occurring during the tests. This phenomenon, which is observed when copper is sputtered in the presence of molybdenum, iron or tantalum, tends to change the sputtering rate of the surface substantially from the value that would normally be expected. The velvet-like appearance of



EFFECT OF TARGET TEMPERATURE ON SPUTTERING RATE

FIGURE 18

layers remaining on the higher temperature detectors and the sputter resistant nature of these layers are consistent with the observed properties of surfaces on which cone formation has occurred. Two conflicting temperature dependent mechanisms can be envisioned which are probably operating during the sputtering process under test here. These are a result of:

- 1) the protective effect of adsorbed mercury which would tend to be present on the lower temperature detectors and
- 2) the protective coneing effect which would tend to be present on the higher temperatures samples. Wehner<sup>[17]</sup> postulates that coneing is enhanced at higher temperatures because the growth of cones requires the migration of such metals as tantalum, molybdenum or iron on a copper surface and this migration is enhanced at higher temperatures.

While it may be possible to select test durations, layer thicknesses and test materials in such a way that the multilayer erosion samples can be employed to determine erosion rates under the test conditions described here, it must be concluded from these results that the multilayer erosion samples used in studies to date cannot be used to obtain quantitative results. The fact that cones are produced from multilayer samples such as these suggests that it may be possible to fabricate sputter erosion resistant components through layering techniques in addition to the alloying technique suggested by Wehner.

## CATHODE IGNITION USING RADIO FREQUENCY POWER

Mercury hollow cathode discharges are presently initiated by heating the cathode with a resistance heater to a sufficiently high temperature so that thermionic electron emission will occur or by creating electrons using a capacitor discharge to create a high voltage, capacitor breakdown in the vicinity of the cathode.<sup>[19]</sup> Additional startup techniques could employ radio-frequency (rf) power to either 1) ionize the mercury vapor and facilitate the establishment of an a.c discharge directly or 2) heat the cathode to thermionic emission temperatures. This study was undertaken to investigate the feasibility of using each of these rf approaches in achieving cathode startup.

### Apparatus and Procedure

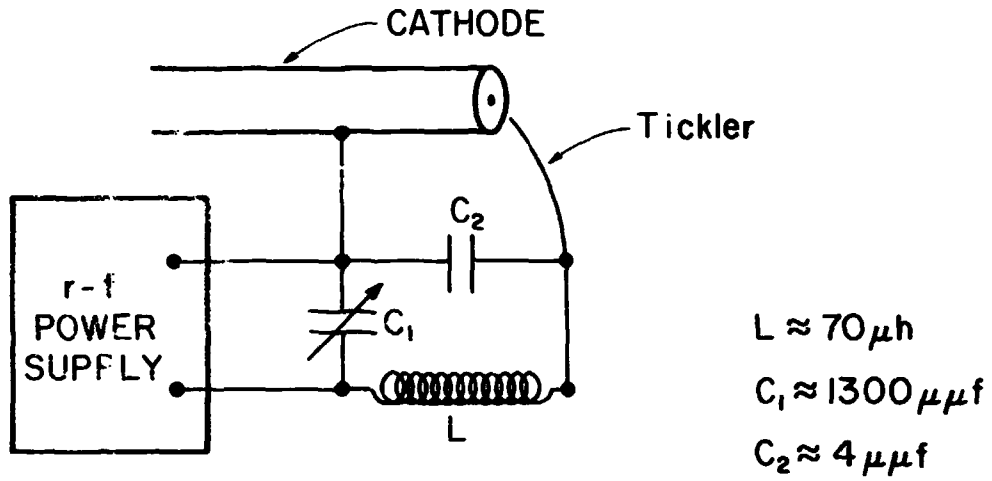
A 6.35 mm diameter hollow cathode with a 0.38 mm wall thickness electron-beam welded to a 1.22 mm thick, 2% thoriated tungsten disc having a 0.76 mm diameter cylindrical orifice was used for this test. It contained a (Semicon type 84-S) porous tungsten hollow cylindrical insert (1.27 cm long x 5.3 mm od x 2.5 mm id) located against its orifice plate. Tests were all conducted in a 30 cm diameter bell jar facility in which the pressure was in the mid-to-high  $10^{-4}$  torr range during testing.

A keeper electrode, maintained at 300 V positive of the cathode potential prior to discharge initiation, was located 1.5 mm downstream cathode orifice plane. The keeper power supply was connected to the keeper through a series resistor which limited the keeper current to 0.5A when the keeper-cathode discharge ignited.

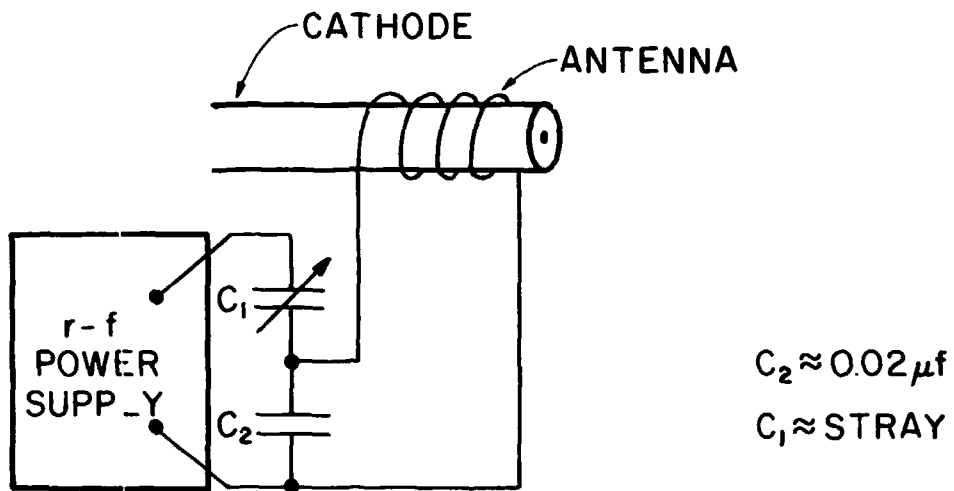
After some analysis and bench testing the resonant circuit of Figure 19 A was settled upon as suitable to achieve the voltage amplification which would effect an electrical breakdown between the cathode and tickler and subsequent ignition. The rf power supply used in the study had both variable power (0 to 100W nominal) and variable frequency (15kHz to 20 MHz) capabilities. The capacitor  $C_1$  was mounted outside of the vacuum chamber so it could be adjusted to achieve impedance matching. The 4  $\mu\text{f}$  capacitor  $C_2$  and the 70  $\mu\text{h}$  rf inductor L were both located within the bell jar in the vicinity of the cathode.

The antiresonant circuit of Figure 19 B employed the same rf power supply to achieve high currents through the antenna shown. Through adjustment of the power supply frequency, this antenna could be made to couple with the cathode thereby effecting the currents at the surface of the cathode tube which heated it. The antenna was a 4 turn coil of 2.1 mm diameter copper wire wound with an 8 mm inside diameter, and both it and the 0.02  $\mu\text{f}$  radio-frequency, high-current capacitor shown in Figure 19 B, were located within the vacuum chamber. Although the capacitance  $C_1$  was required for impedance matching for low power bench tests, the antiresonant circuit impedance was near that of the power supply, when cathode heating was being effected, and  $C_1$  could be reduced to near zero.

The tests were conducted by heating the tubes leading to the cathode above the mercury condensation temperature ( $\sim 150^\circ\text{C}$ ), establishing the desired cathode flow rate and applying a +300 V potential to the keeper. In the case of high voltage breakdown tests the desired cathode tip temperature was also established and initiation of the keeper discharge was then attempted.



A. r-f HIGH VOLTAGE BREAKDOWN CONFIGURATION



B. r-f INDUCTIVE HEATING CONFIGURATION

CATHODE STARTUP CIRCUITS

FIGURE 19

## Results

At cathode tip temperatures of 400°C and above and with mercury flow rates of 200 mA and greater, cathode startup could be achieved repeatedly with the high voltage breakdown test configuration of Figure 19 A. This breakdown occurred at a frequency of ~2.5 MHz, a net rf power load of less than 20W and a peak-to-peak voltage across capacitor  $C_1$  of 400 V. Bench tests suggest this corresponds to a voltage across capacitor  $C_2$  of 11 kV (peak-to-peak), although direct measurements of this breakdown voltage were not made during the actual test. Attempts to initiate the discharge when the cathode tip temperature was below 400°C would result in rf breakdown between the cathode and tickler, but the keeper discharge would not ignite. At cathode flow rates below 200 mA rf breakdown could not be achieved because breakdown would begin to occur across insulators rather than the cathode-tickler gap. Insulators posed a significant problem during this test in that application of voltages of 400 V peak-to-peak across  $C_1$  resulted in insulator heating with an attendant power drain from the circuit. The insulators could on occasion be seen glowing red and occasionally they would fail mechanically. Application of voltages just below values required for rf breakdown would also eventually (tens of seconds) result in insulator heating and a concomitant power drain. Once the insulators were hot the rf power had to be turned off and they had to be allowed to cool before startup could be effected again. It is believed that much more efficient startup could have been achieved over a wider flow rate and temperature range if proper insulators had been used.

Ignition of the keeper discharge was also observed to occur with the circuit of Figure 19 A at a frequency of 7.7 MHz when tip temperatures were

greater than 300°C and cathode flow rates were greater than 50 mA. In this case breakdown would occur within the 70  $\mu$ h inductor and a few seconds later the keeper-cathode discharge would ignite. In these cases no discharge was visible between the tickler and the cathode before the keeper discharge started. Once the keeper discharge had started by either of the above mechanisms, the keeper voltage could be reduced to zero and the rf tickler-cathode discharge could be maintained indefinitely using about 1 watt of rf power for flow rates above 50 mA and tip temperatures above 300°C. The keeper discharge could be restarted at will from this discharge by simply increasing the keeper voltage.

The inductive heater illustrated in Figure 19 B was also found to facilitate cathode startup. At a frequency of 3.1 MHz and a net level of 110 watts the cathode tip could be heated from ambient temperatures to 1200°C in 15 seconds. At a cathode flow rate of about 100 mA the keeper discharge would then ignite readily. During rf heating, the wall of the cathode was observed to heat up in a few seconds and the remainder of the time was apparently required for heat conduction to occur from the tube to the orifice plate and insert. It appeared that once the temperatures of these cathode parts reached sufficiently high values ignition occurred.

The cathode used in this study was bare and the radiation from it was very intense. Although no attempt was made to insulate it, it is believed that the power required for heat up could have been reduced substantially if a ceramic tube had been placed around the tube to provide some degree of insulation against radial heat loss. Once the keeper discharge had started, its voltage could be lowered to zero and a discharge which appeared very much like a conventional keeper discharge could be maintained using

about 20 watts of rf power to the coil. Although this rf discharge could not be induced with the rf coil alone, it was possible to start it with a high voltage pulse between the cathode and a tickler electrode. This suggests that it might be possible to eliminate the keeper and accomplish its cathode sustaining and starting functions using an rf coil and high voltage ignitor.

#### Conclusion

Approximately 100 watts of radio-frequency power is sufficient to heat a bare cathode inductively to a sufficiently high temperature to effect ignitor of a cathode-keeper discharge within about 15 seconds. High voltage radio-frequency signals can also be used to initiate a high voltage breakdown between a tickler electrode and the cathode. Both of these circuits can also be used to sustain a cathode discharge after the keeper has been turned off.

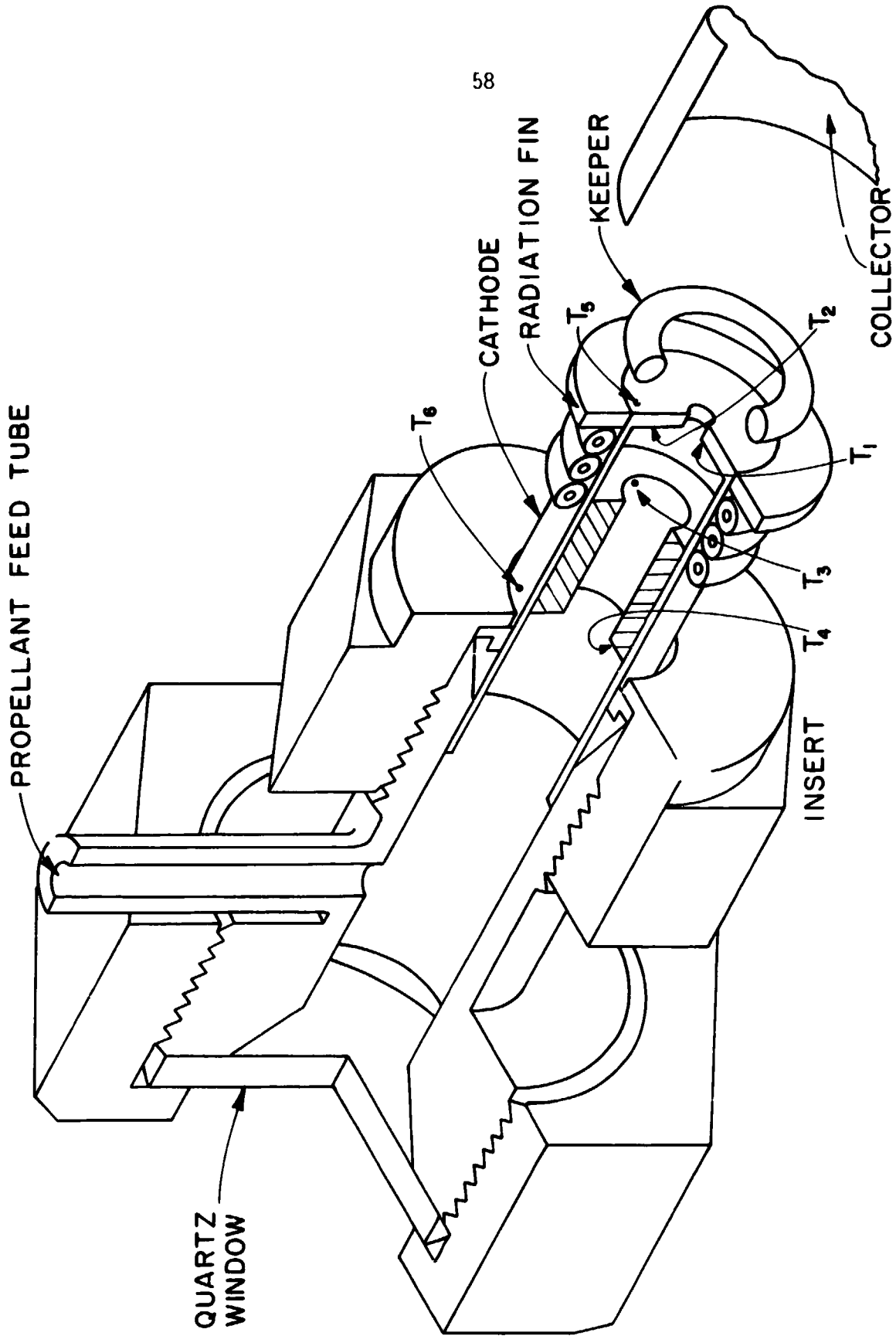
## THE EFFECT OF THE INSERT ON HOLLOW CATHODE TEMPERATURES

Dan Siegfried

The lifetime of a hollow cathode, which is determined by its capacity to emit electrons without excessive keeper voltages, is generally determined by erosion in the cathode orifice and depletion of the low work function material supplied by the cathode insert.<sup>[20]</sup> Both of these limitations are temperature related. A high temperature in the cathode orifice region is indicative of a high ion sputtering rate and rapid erosion of the orifice. Mirtich and Kerslake<sup>[21]</sup> have shown that insert temperature on the other hand determines the rate of release of low work function material. A low insert temperature will result in a low release rate, high cathode work functions and excessive voltages and erosion rates. A high insert temperature will result in an excessive release rate and premature depletion of the low work function material. The effects of insert type, insert position, orifice size, emission current and cathode heater power on the cathode and insert temperatures are however not well known. The objective of this study has been the determination of the effects of variations in these insert and cathode parameters on cathode and insert temperatures.

### Apparatus and Procedure

All tests were made on a hollow cathode composed of a 6.35 mm diameter tantalum tube with a 0.38 mm wall thickness electron beam welded to a 1.22 mm thick, 2% thoriated tungsten disc. The disc had an orifice on its centerline and was mounted on a viewing structure in the manner illustrated by the cutaway sketch of Figure 20. The insert shown in the figure was impregnated with low work function material and could be positioned at various



CATHODE AND VIEWING STRUCTURE

FIGURE 20

axial positions from zero to 4 mm upstream of the orifice plate. It was electron beam welded to a pigtail wire which was in turn spot welded to the viewing structure to effect good electrical contact during cathode operation. The radiation fin shown, while it was held only by friction onto the cathode, did enhance heat transfer from the orifice plate. The radiation fin, used in conjunction with the cathode heater shown upstream of it in Figure 20, facilitated cathode operation over a wide range of cathode temperatures at any given cathode emission current level. This capability was considered essential to model the wide range of heat transfer environments which could be encountered in hollow cathode applications.

Temperatures on the interior surfaces of the cathode and insert were measured using a micro optical pyrometer which was sighted through the quartz window shown in Figure 20. Using this device the following temperatures were measured at the locations indicated on the figure:

- $T_1$  - At the edge of the orifice
- $T_2$  - On the orifice plate at the inside radius of the insert
- $T_3$  - On the insert at the interior downstream edge
- $T_4$  - On the upstream end of the insert.

The temperatures  $T_5$  (on the outside of the orifice plate) and  $T_6$  (on the outside of the cathode tube upstream of the heater) were sensed by platinum/platinum-rhodium thermocouples.

The effect of cathode orifice diameter was examined in this test by making measurements in cathodes having orifice diameters of 0.38 mm, 0.76 mm and 1.02 mm. Three different (Semicon type 84-S) cylindrical inserts having the dimensions given below were used within the cathode.

Table V

## Cathode Insert Dimensions

Insert Designation	Inside Diameter	Outside Diameter	Length
A	3.8 mm	5.3 mm	12.7 mm
E	2.5 mm	5.3 mm	12.7 mm
D	(Solid)	1.9 mm	12.7 mm

Temperature measurements were taken over a range of emission currents with each of these inserts positioned against, 2 mm upstream and 4 mm upstream of each of the orifice plates investigated.

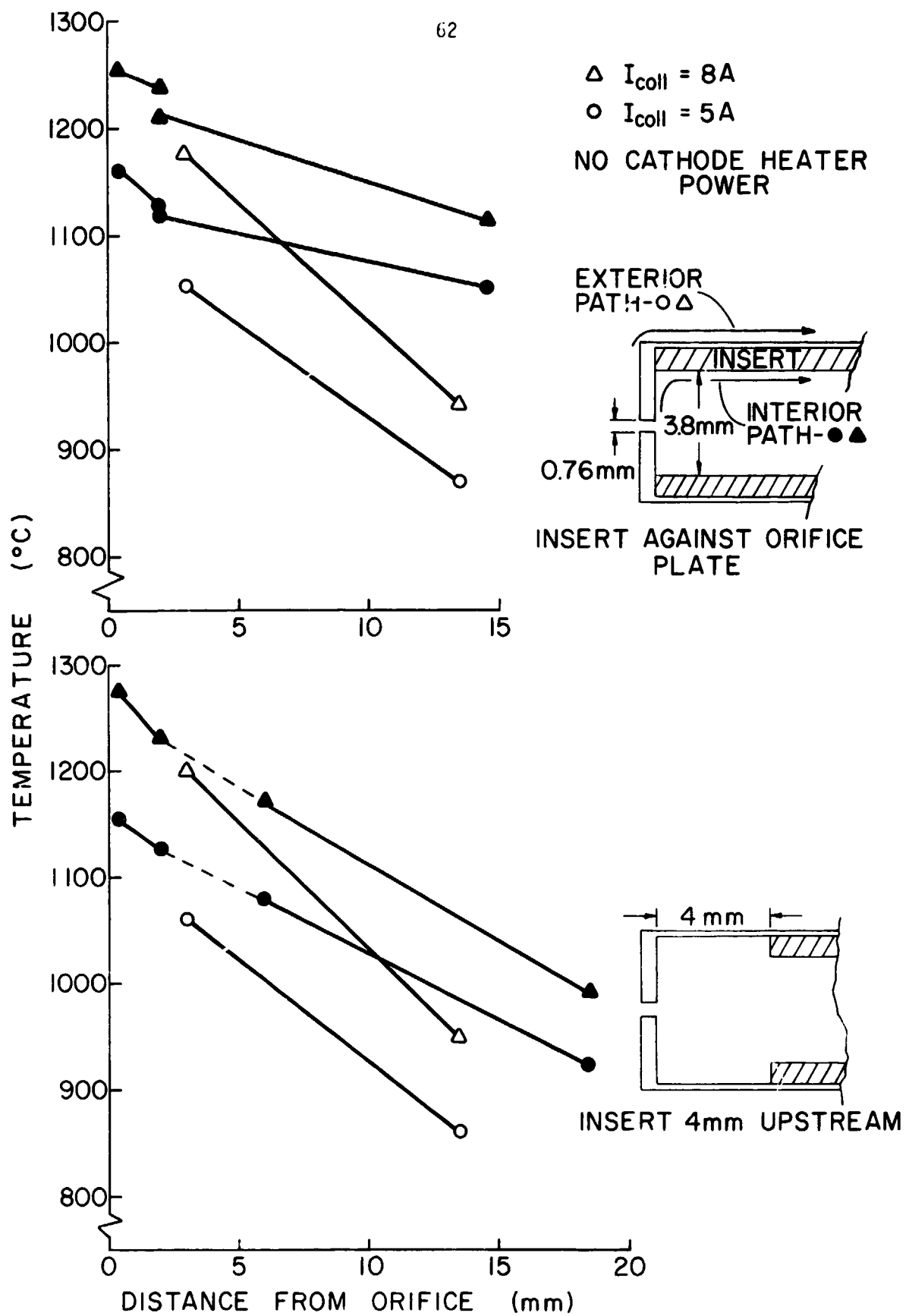
The tests were conducted in a vacuum bell jar facility. During their conduct, the cathode flow rate was maintained at approximately 150 mA and the keeper current at 0.3 A. Prior to each test the insert was subjected to a break-in period of at least 30 minutes during which time the cathode was operated at an emission level of about 3 A while the tip temperature ( $T_5$ ) was maintained at about 1000°C. At the conclusion of the break-in period the temperatures  $T_1$  to  $T_6$  were stable and could be recorded reproducibly. The collector current was subsequently increased as cathode heater power was reduced to maintain a constant tip temperature ( $T_5$ ) of 1000°C and temperature data were again recorded. This procedure was repeated at several collector currents and at cathode heater powers ranging from zero to 60 watts. Tip temperatures of 1050°C, 1100°C, 1150°C and 1200°C were subsequently established and temperature data were collected over a range of collector currents at each tip temperature state. After collection of these data the cathode was allowed to cool to ambient temperatures before the insert position, insert type or cathode was changed.

Between tests inserts were stored under vacuum conditions to prevent degradation.

### Results

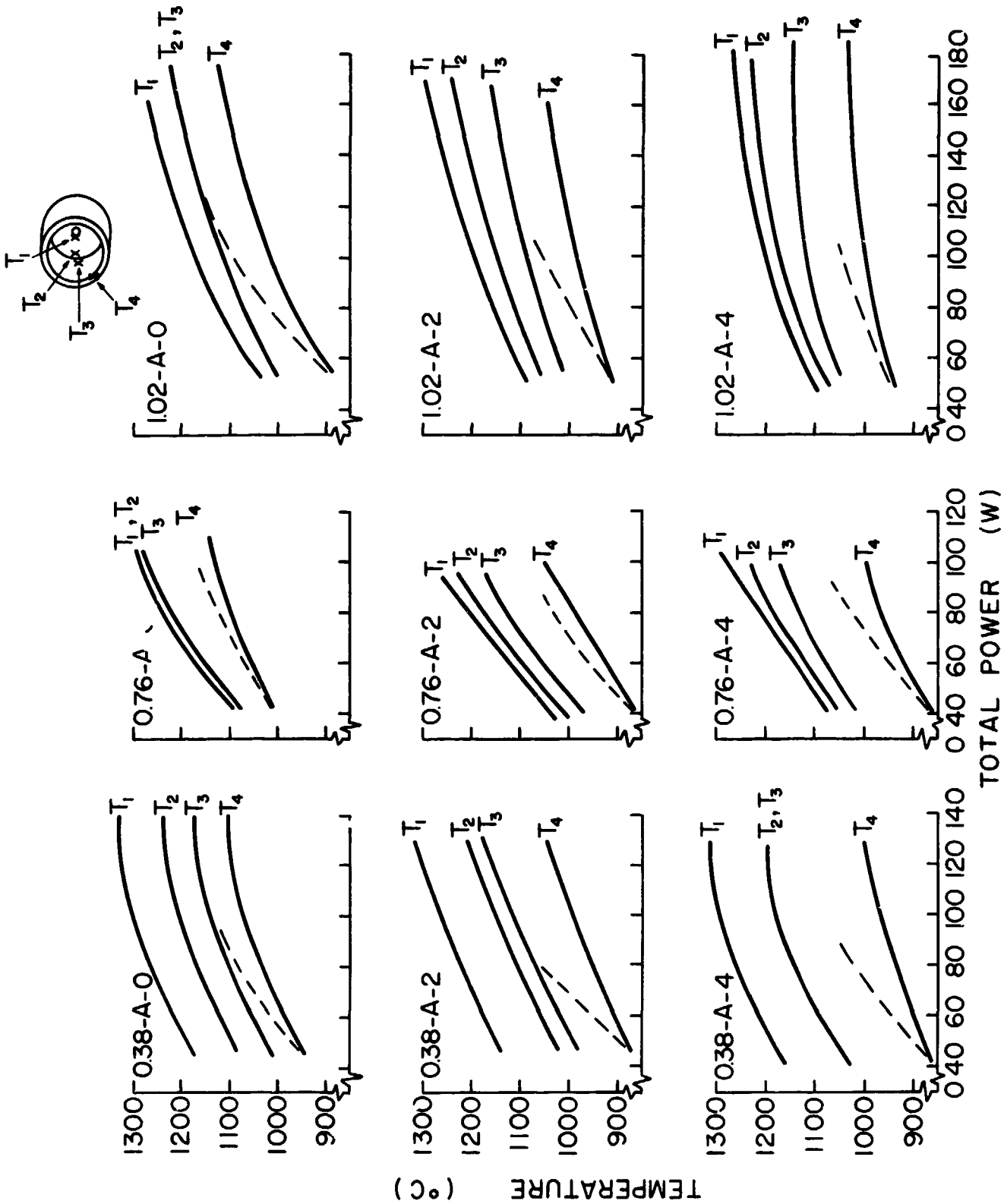
Temperature measurements yielded results like those shown in Figure 21. These particular data were obtained with the "A" insert located against and 4 mm upstream of an orifice plate having a 0.76 mm dia. orifice with collector currents of 5A and 8A and no cathode heater power. These data show: 1) interior temperatures (solid symbols) are higher than the exterior temperatures (open symbols), 2) temperatures are highest at the orifice and they decrease monotonically with distance from the orifice, 3) temperatures are increased at all locations with increases in emission current and 4) moving the insert 4 mm upstream results in a decrease in its temperature. upstream results in a decrease in its temperature.

Extensive data of the sort presented in Figure 21 were obtained as a function of the variables described. Presenting this information in a logical and useful form posed a challenge until it was discovered that temperatures; measured with a given orifice, insert type and insert position over a wide range of currents and cathode heater powers; correlated well with total power (i.e. the sum of cathode heater power, the collector current-voltage product and the keeper current-voltage product). Plots of temperatures within the hollow cathode against total power are presented in Figure 22 for the "A" insert (described in Table V). The locations at which temperatures were measured on the insert and the orifice plate are again defined by the inset on this Figure. The designation given for each plot defines: the orifice diameter (mm)--insert type--orifice plate/insert



CATHODE TEMPERATURE PROFILES

FIGURE 21

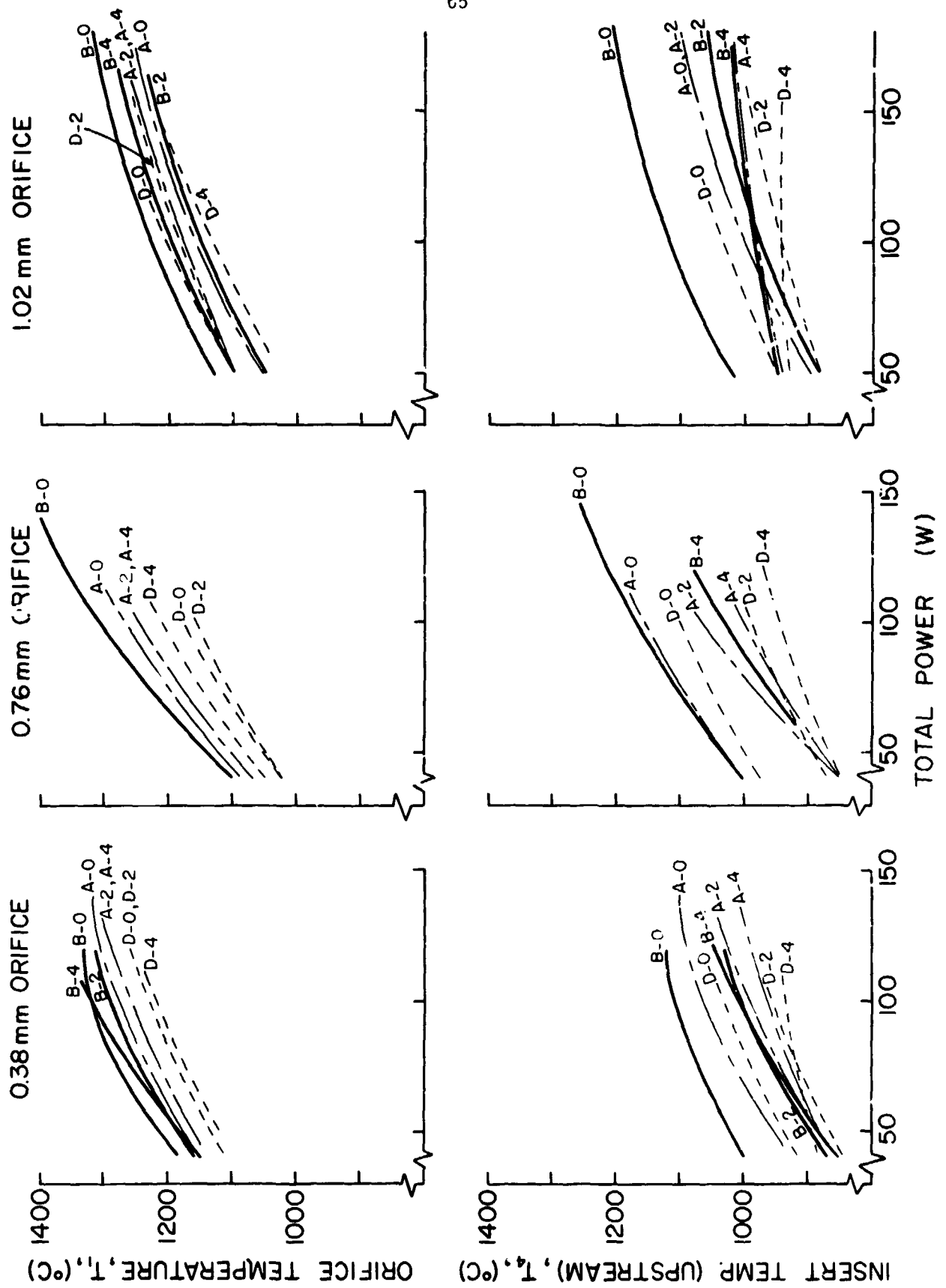


EFFECTS OF TOTAL POWER ON CATHODE TEMPERATURES

FIGURE 22

separation distance (mm) pertaining to that plot. Thus the lower left hand plot (0.38-A-4) shows the variation in temperature for the 0.38 mm dia. orifice cathode equipped with the "A" insert located 4 mm upstream of the orifice plate. Typically the data points scattered randomly within  $\pm 25^\circ\text{C}$  around the lines defining the temperatures  $T_1$ ,  $T_2$  and  $T_3$  in Figure 22. In the case of the temperature at the upstream end of the insert ( $T_4$ ) the scatter was greater and a systematic variation of temperature with cathode heater power was evident. Two lines are therefore used to bracket these temperature measurements, a solid line corresponding to temperatures at low cathode heater power and a dotted one corresponding to the high cathode heater powers. The sensitivity of temperature at the upstream end of the insert to cathode heater power is to be expected because this end of the insert is in much better thermal communication with the cathode heater than it is with the seat of discharge power deposition at the cathode orifice.

The data of Figure 22 all show the expected decrease in temperature as one moves away from the cathode orifice. In addition the shapes of the  $T_1$ ,  $T_2$ ,  $T_3$  and the zero cathode heater power  $T_4$  (solid line) curves are similar. It should be pointed out however that there is some uncertainty associated with the measurement of  $T_2$  and  $T_3$  which makes it futile to attempt to draw too many conclusions from these data. These uncertainties are introduced because: 1) the measurement of  $T_4$  requires viewing of the insert surface at a grazing angle and variations in temperature readings are observed as this viewing angle is varied. 2) The measurement of both  $T_2$  and  $T_3$  requires viewing through the region close to the hot barium impregnated insert. Barium produces line radiation at red wave lengths which can perturb color temperature measurements made with the red-sensitive pyrometer. In view of



EFFECT OF INSERT ON TEMPERATURES

FIGURE 23

these possible errors the orifice temperature ( $T_1$ ) and the upstream insert temperature ( $T_4$ ) were selected as most reliable. In all data recorded the  $T_1$  and  $T_4$  data straddled the  $T_2$  and  $T_3$  data and examination of the two temperatures therefore enables one to bound the  $T_2$  and  $T_3$  temperatures.

Figure 23 presents the temperature  $T_1$  and  $T_4$  as a function of total power for all of the insert types and positions and orifice diameters investigated. The designations on each line represent the insert type (A, B or D as defined in Table V) and its separation distance from the orifice plate in millimeters. The upstream insert temperature ( $T_4$ ) plotted in Figure 23 is the one corresponding to zero cathode heater power (solid lines in Figure 22).

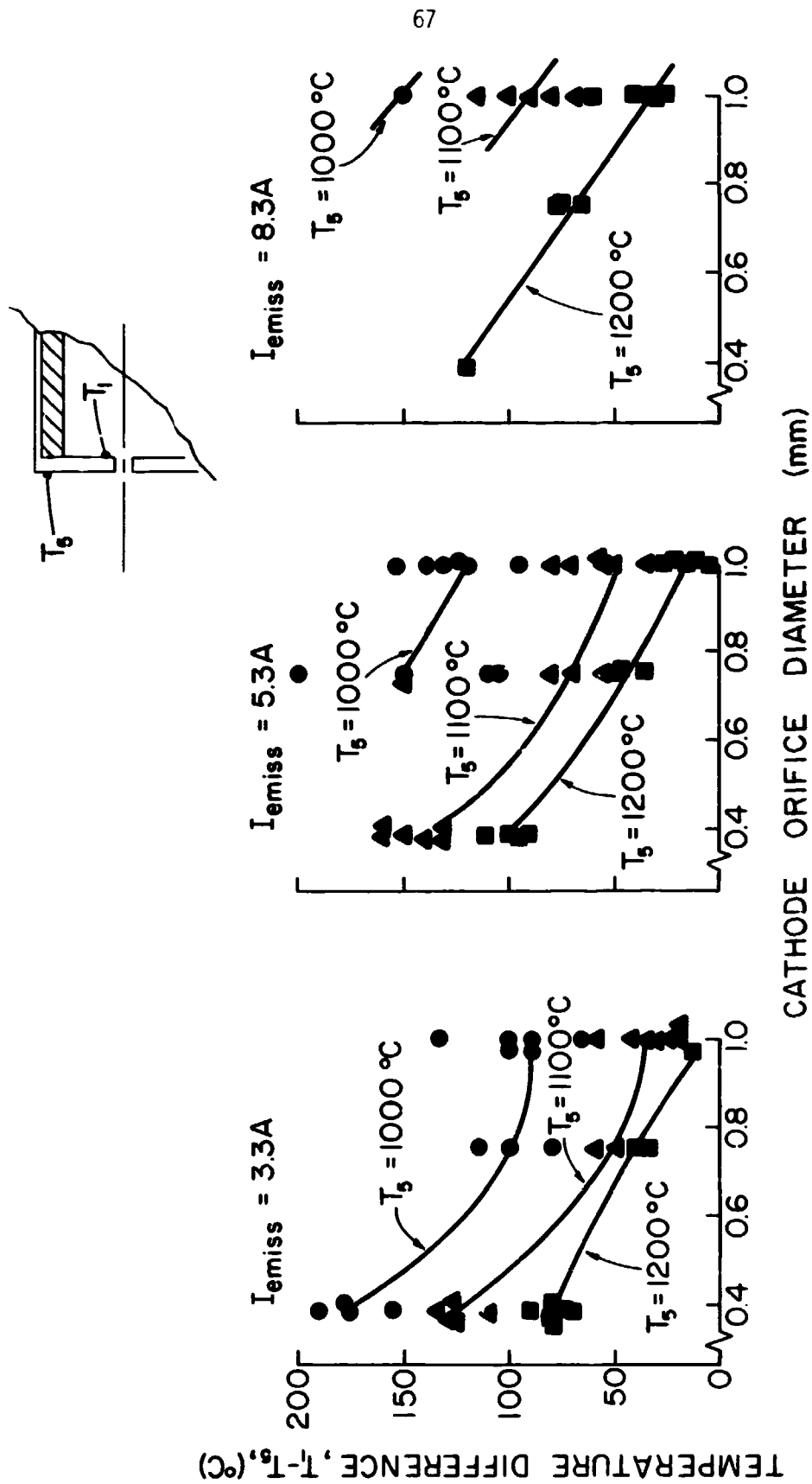
Although it is difficult to generalize based on the data of Figure 23 because exceptions are plentiful the following appear to hold most of the time: 1) the highest temperatures are observed in the "B" insert and the lowest in the "D" insert. Since insert "B" has the greatest cathode wall-to-plasma exposed area ratio and "D" has the lowest value of this ratio, these results support a theory which proposes this ratio as a temperature correlating parameter.\* 2) Temperatures generally decrease as the insert

---

\* A logical cathode model might presume cathode arc power is deposited at the orifice and then transferred in significant amounts by conduction to the cathode tube. An energy balance would then show the insert receiving the bulk of its power by radiation from the cathode tube wall (proportional to insert area seeing the surface) and losing power as a result of electron liberation (proportional to the insert area exposed to the plasma). Such a model would support the ratio of surface area seeing the tube wall to surface area seeing the plasma as the significant parameter.

ORIFICE PLATE THERMAL GRADIENTS

FIGURE 24



is moved further upstream with the decrease between the flush and 2 mm position being greater than that for the 2 mm to 4 mm position change.

3) The range of orifice temperature variations which can be effected by the changes in insert location and type considered here lies in the range of 100°C for all total power levels investigated. 4) The range of upstream insert temperature variations which can be effected by changes in insert type and position, varies from about 100°C at low cathode powers to 200°C to 300°C at high total power levels.

It is desirable to relate the temperature measured on the outside of the cathode orifice plate to a temperature on the inside. This correlation is presented in Figure 24 where the temperature difference between the interior orifice region and the exterior cathode edge ( $T_1 - T_5$ ) is plotted as a function of cathode orifice diameter for three different cathode emission currents. The curves pertain to all insert types and positions. The parameter in these curves is the temperature  $T_5$ . The three different values of  $T_5$  were achieved at the same orifice diameter and emission condition by varying cathode heater power. Although the data show considerable scatter they exhibit consistent trends. The temperature difference at a given value of  $T_5$  increases with increasing emission (keeper plus collector) current and with decreasing cathode orifice diameter. The decrease in the temperature difference with increases in  $T_5$  is caused by the cathode heater power increase which tends to increase  $T_5$ . The temperature differences suggested by Figure 24 are indeed large, but analysis reveals that temperature differences of this order could be sustained if a sizeable fraction of the cathode discharge power were deposited at the interior surface of the orifice. A thermal model of cathode operation in which the cathode

discharge power is presumed to be deposited in the orifice would be consistent with the observed variations in temperature difference as a function of orifice diameter, cathode heater power and emission current of Figure 24.

### Conclusions

Temperatures measured within a hollow cathode during operation tend to correlate with total cathode power (sum of cathode heater power and the emission current-keeper voltage product for a thruster cathode). Cathode orifice plate and insert temperatures can be reduced on the order of 100°C by moving the cathode insert upstream and/or by reducing the cathode wall-to-plasma exposed area ratio of the insert. Temperature differences measured between the edge of the orifice and the outer edge of the orifice plate can be of the order of 100°C. Sustaining this magnitude of temperature difference would require that a substantial fraction of the cathode discharge power be deposited at the cathode orifice.

APPENDIX A  
MAGNETIC BAFFLE FOR  
15 cm MULTIPOLE MERCURY THRUSTER

G. Reed Longhurst

Initial testing of the 15 cm multipole mercury thruster demonstrated the following significant effects which influence the design of the cathode chamber: 1) when the non-magnetic baffled cathode chamber aperture was near the center pole piece at the upstream end of the thruster (Figure 4), electrons could tend to become trapped by the magnetic lines of force located there. This caused a disproportionately large fraction of the ionization within the main discharge chamber to occur near one anode (the innermost upstream one) and correspondingly poor performance. To reduce this effect, the cathode chamber was moved downstream to a point where the magnetic fringe fields of the upstream pole pieces would not capture the primary electrons coming from the baffle aperture. 2) When the thruster was operated with the baffle aperture at this downstream location, the discharge voltage was below that required for good thruster performance. This low discharge voltage was observed to occur for a variety of baffle aperture areas and locations.\* Based on these results and difficulties encountered during

---

\* Generally a high discharge voltage was accompanied by a high keeper voltage, a high cathode discharge plasma potential and severe ion impingement on the cathode. At some cathode flow conditions the keeper voltage could be reduced to acceptably low values, while discharge voltage remained high, but in these cases the plasma potential in the main discharge chamber was low and a large voltage drop occurred across the plasma sheaths at the anodes.

startup with very small apertures it was concluded that the addition of a variable field strength magnetic baffle would be required.

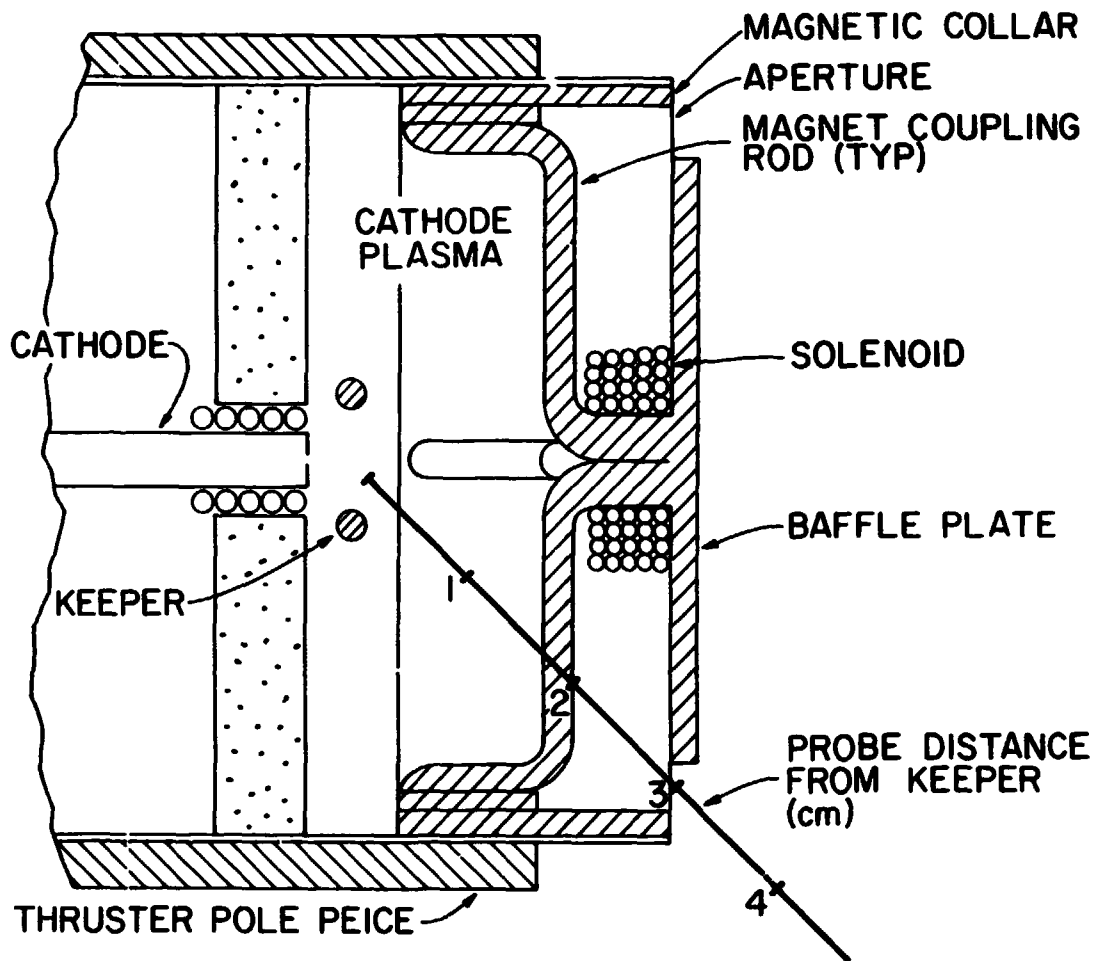
### Baffle Design

Previous magnetic baffle designs have established a field between a cathode pole piece and a magnetic baffle plate through the use of solenoidal windings located outside of the cathode chamber. [22, 9] The magnetic circuit from the pole piece to the baffle plate is completed by a slotted tube or rods which also supports the baffle plate. That approach was unsatisfactory for the present application because of the need to move the baffle/cathode assembly, relative to the upstream innermost pole piece during thruster operation, to optimize the thruster design with respect to the point of electron injection.

The baffle design which evolved is shown schematically as Figure A-1. The magnetic circuit is completed through the baffle plate, coupling rods and magnetic collar across the aperture as illustrated. The magnetic field perpendicular to the path shown as the heavy line in Figure A-1 tends to peak sharply at the aperture location (3 cm from the keeper). This peak magnitude of the component of field strength perpendicular to the probe path, shown in Figure A-1 is designated  $B_0$ .

### Testing

To determine if sufficient aperture impedance could be achieved with the baffle design of Figure A-1, before actually installing it in a thruster, the upstream end of the thruster with the magnetic baffle was placed in a 30 cm bell jar facility. The main discharge plasma was simulated by coupling the efflux of the cathode chamber to a wire loop anode 5 cm in diameter and 2 cm downstream from the baffle aperture. A movable Langmuir



MAGNETIC BAFFLE SCHEMATIC

Showing Locus of Probe Locations

Where Plasma Properties were Measured

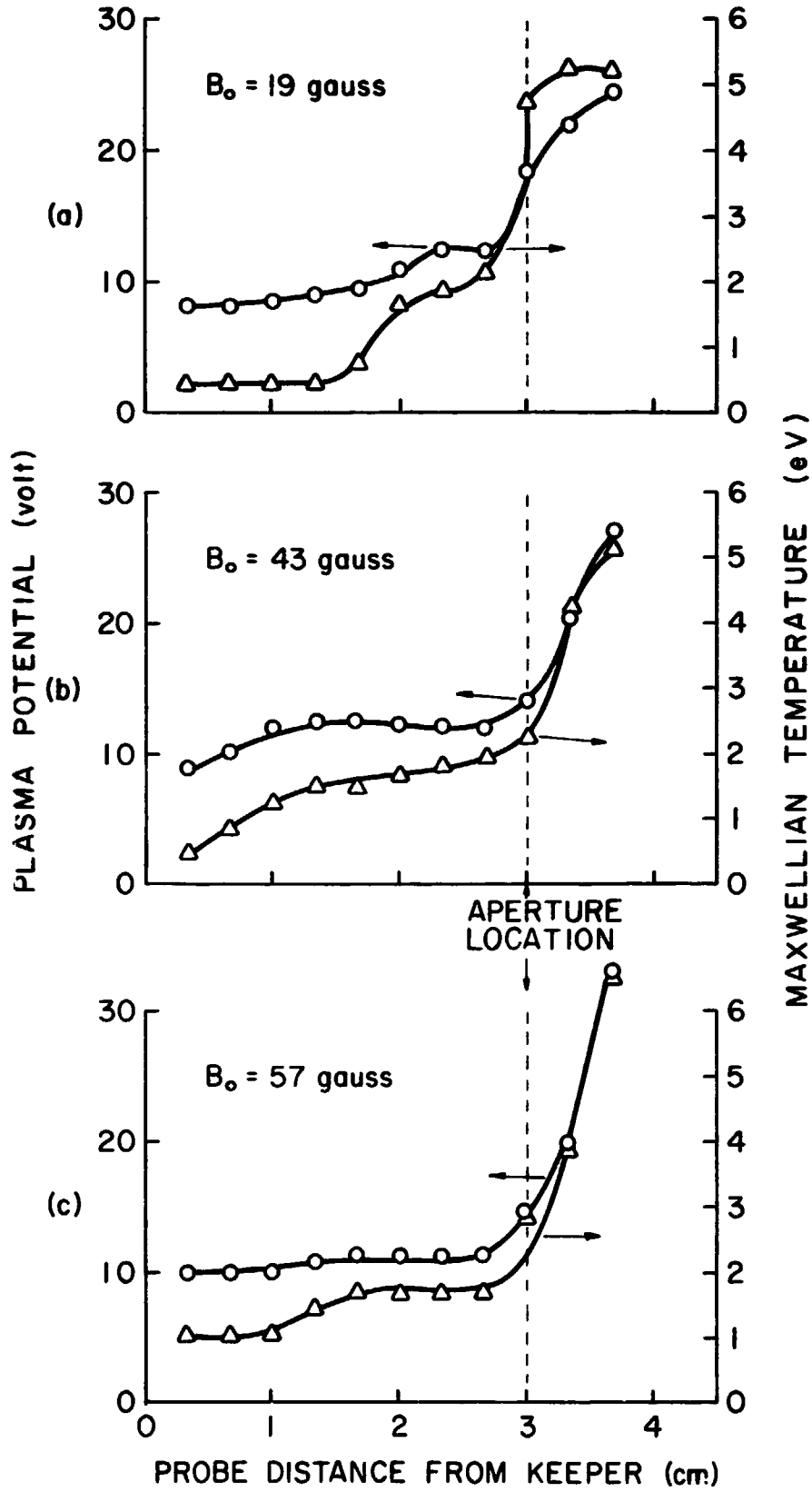
FIGURE A-1

probe was inserted through the orifice toward the keeper along the path shown in Figure A-1. At an ambient pressure of about  $10^{-3}$  torr a discharge was established in the cathode chamber over a range of mass flow rates ranging from 160-330 mA. The device was operated with the cathode chamber extended 0, 1 and 2 cm from the thruster upstream pole piece plane, and at varying main and baffle magnet current combinations.

### Results

Graphical analysis of Langmuir probe traces taken along the path shown in Figure A-1, was used to estimate plasma potential and Maxwellian electron temperature as a function of position. It was found that while plasma potentials were somewhat lower than desired, they were significantly better than those achieved with the non-magnetic baffle. Figure A-2 shows the plasma potential and Maxwellian temperature measured for 3 typical cases corresponding to magnetic field intensities at the aperture ( $B_0$ ) of 19, 43, and 57 gauss. Several features of these curves are of interest.

First it is observed that within the cathode chamber near the keeper, the plasma potential is 6-8 V above the keeper potential. That is expected since the keeper is the most positive surface in the region, and the Bohm criterion requires the plasma to be somewhat positive of that. The plasma potential does not vary significantly from that value until one approaches the vicinity of the baffle aperture. Here it appears the electrons begin to be influenced by the potential outside the chamber. A comparison of the three data sets of Figure A-2 shows that when the baffle magnet strength ( $B_0$ ) is least, the greatest departure from this general behavior occurs. In fact, an increase in temperature and plasma potential occurs near the coupling rod (-2 cm) for the 19 gauss case. When the baffle magnetic field



EFFECT OF BAFFLE APERTURE MAGNETIC FIELD

ON PLASMA PROPERTIES

FIGURE A-2

is strong, plasma potential within the chamber is most uniform. Finally it is observed from Figure A-2 that in the higher magnetic field cases ( $B_0 = 43$  and  $57$  gauss) much of the increase in plasma potential and electron energy occurs downstream of the aperture whereas it occurred in the aperture itself for the  $19$  gauss field. It is desirable to effect primary electron acceleration downstream of the aperture so energy imparted to the electrons is not lost during passage through the aperture. The increase in plasma potential downstream of the aperture in the higher field intensity cases would correspond to this operating condition.

Following bell jar testing of the baffle assembly of Figure A-1, it was installed in the thruster and it operated satisfactorily, producing the impedance control necessary to insure proper thruster operation.

## REFERENCES

1. King, H. J., et al, "2½ kW Low Specific Impulse, Hollow Cathode Mercury Thruster," AIAA Paper No. 69-300, March 3-5, 1969.
2. Beattie, J. R., "Cusped Magnetic Field Mercury Ion Thruster," NASA CR-135047, July 1976.
3. Wells, A. A., "Current Flow Across a Plasma 'Double Layer' in a Hollow Cathode Ion Thruster," AIAA Paper No. 72-418, April 17-19, 1972.
4. Peters, R. R., "Double Ion Production in Mercury Thrusters," NASA CR-135019, April 1976.
5. Hudson, Wayne R., "Auxiliary Propulsion Thruster Performance with Ion Machined Accelerator Grids," AIAA Paper 75-425, March 19-21, 1975.
6. Byers, David C. and John F. Staggs, "SERT II Flight-type Thruster System Performance," AIAA Paper No. 69-235, March 3-5, 1969.
7. Wilbur, P. J., "An Experimental Investigation of a Hollow Cathode Discharge," NASA Cr-120847, December 1971.
8. Vahrenkamp, R. P., "Measurement of Doubly Charged Ions in the Beam of a 30-cm Mercury Bombardment Thruster," AIAA Paper No. 73-1057, Oct. 31 - Nov. 2, 1973.
9. Manteniaks, M. A. and V. K. Rawlin, "Sputtering Phenomena of Discharge Chamber Components in a 30-cm Diameter Hg Ion Thruster," AIAA Paper No. 76-988, Nov. 15-17, 1976.
10. Isaacson, G. C. and H. R. Kaufman, "15 cm Multipole Gas Ion Thruster," AIAA Paper 76-1045, Nov. 14-17, 1976.
11. Beattie, J. R., "Numerical Procedure for Analyzing Langmuir Probe Data," AIAA Journal, Vol. 13, No. 7, July 1975, pp. 950-952.
12. Wilbur, P. J., "Experimental Investigation of a Throtttable 15 cm Hollow Cathode Ion Thruster," NASA CR-121038, December 1972.
13. Robirson, R. S. and H. R. Kaufman, "Application of Ion Thruster Technology to a 30-cm Multipole Sputtering Ion Source," AIAA Paper No. 76-1016, Nov. 14-17, 1976.
14. Aston, Graeme, "The Ion Optics of a Two-grid Electric-Bombardment Thruster," NASA CR-135034, May 1976.
15. Kaufman, Harold R., "Accelerator-System Solutions for Electron-Bombardment Ion Sources," AIAA Paper No. 75-430, March, 1975.

16. Kaminsky, Manfred, Atomic and Ionic Impact Phenomena on Metal Surfaces, pp. 163-164, Academic Press, New York, 1965.
17. Wehrer, G. K. and D. J. Hajicek, "Cone Formation on Metal Targets during Sputtering," Journal of Applied Physics, Vol. 42, No. 3, 1 March 1971.
18. Free, B. A., et al., "Effect of a Decel Electrode on Charge Exchange Erosion Pattern in an Ion Thruster," IIIrd European Electric Propulsion Conference, Hinterzarten, Federal Republic of Germany, October 14-18, 1974.
19. Wintucky, E. G., "High Voltage Ignition of Mercury Discharge Hollow Cathodes," AIAA Paper No. 73-1140, Oct. 31 - Nov. 2, 1973.
20. Mirtich, M. J., "Investigation of Hollow Cathode Performance for 30-cm Thruster," AIAA Paper No. 73-1138, Oct. 31 - Nov. 2, 1973.
21. Mirtich, M. J. and W. R. Kerlake, "Long Lifetime Cathodes for 30-cm Mercury Ion Thruster," AIAA Paper 76-985, Nov. 14-17, 1976.
22. Poeschel, R. L. and W. Knauer, "A Variable Magnetic Baffle for Hollow Cathode Thrusters," AIAA Paper 70-175, Jan., 1970.